Non-Standard Search for Dark Matter with CRESST

DISSERTATION

der Mathematisch-Naturwissenschaftlichen Fakultät
der Eberhard Karls Universität Tübingen
zur Erlangung des Grades eines
Doktors der Naturwissenschaften
(Dr. rer. nat.)

vorgelegt von
VINCENT SCHIPPERGES
aus Heidelberg

Tübingen
2020

Zusammenfassung

Dunkler Materie ist eines der großen Rätsel unserer Zeit. CRESST ist ein Experiment, das darauf abzielt, den von dunkler Materie induzierten Kernrückstoß und damit ihre Existenz nachzuweisen und Rückschlüsse auf ihre Eigenschaften ziehen zu können. Da dieser Nachweis bis heute weder CRESST noch anderen Experimenten gelungen ist, geraten zunehmend Theorien in den Fokus, die von der Standardannahme eines etwa $100\,\mathrm{GeV}/\mathrm{c}^2$ schweren sogenannten WIMPs abweichen, das über einen relativ zum Energieübertrag schweren Mediator und spin-, isospin-, geschwindigkeits- und impulsunabhängig mit Nukleonen interagieren soll.

Insbesondere ist der Schwerpunkt des CRESST-Experiments aufgrund der kleinen, aber genauen Detektoren leichte dunkle Materie mit einer Masse weit unter $10\,\mathrm{GeV}/\mathrm{c}^2$. In dieser Arbeit werden die Messdaten des Experiments im Rahmen einer effektiven Feldtheorie untersucht, bei der die Wechselwirkung zu Nukleonen mit 28 verschiedenen Operatoren (je nach Darstellung je 14 Operatoren für Protonen und Neutronen bzw. für Isoskalar- und Isovektor-Wechselwirkung) beschrieben wird und so mögliche Abhängigkeiten vom Isospin, den Spins der Nukleonen und der dunklen Materie, vom Impulsübertrag, sowie von der relativen transversalen Geschwindigkeit, mit in Betracht gezogen werden.

Die theoretischen Rückstoßspektra für zwei der Hauptbestandteile der CRESST-Detektoren, Sauerstoff-16 und Calcium-40, für sieben verschiedene dieser Operatoren werden in dieser Arbeit berechnet, mit den aufgenommenen Spektra verglichen und somit massenabhngige obere Grenzen auf die Kopplungsstärke gesetzt. Alle diese Limits berschreiten die Sensitivität von bisher publizierten Ergebnissen im Bereich niedriger Dunklen-Materie-Massen unter $3\,\mathrm{GeV}/\mathrm{c}^2$.

Abstract

Dark Matter is one of the large puzzles of our time. CRESST is an experiments trying to prove nuclear recoils induced by dark matter and thus its existance, and to deduce some of its properties. Up until know, no such signal has been proven by CRESST or other experiments. Therefore, a growing emphasis is on dark matter theories that differ from the standard assumption of so-called WIMPs with a mass of around $100\,\mathrm{GeV/c^2}$ that interact with nucleons via a heavy mediator (compared to the energy transfer) and independently of involved spins, isospins, velocities and momenta.

Especially, the focus of the CRESST experiment with its small, but sensitive detectors is light dark matter with a mass of way below $10\,\mathrm{GeV/c^2}$. In this work, experimental data from the experiment is investigated in the context of an effective field theory, where the interaction to nucleons is described with 28 different operators (depending on the reprensentation 14 operators each for protons and neutrons, or for isoscalar and isovector interaction). Possible dependencies on the isospin, spins of the nucleons and of the dark matter, the momentum transfer, as well as the relative transverse velocities are taken into account by these operators.

Theoretical recoil spectra for two of the main components of the CRESST detectors, oxygen-16 and calcium-40, for seven of these operators are calculated in this work and compared to the measured experimental spectra. Mass-dependent upper limits are set on the interaction strength. All of these limits surpass the sensitivity of previously published results for masses below $3\,\mathrm{GeV/c^2}$.

Contents

Chapter 1

Dark Matter

1.1 Evidence

Dark matter has been proposed in the 1930s by astronomer Fritz Zwicky[1]. He measured the Doppler shifts, determined the velocities of galaxies within the Coma Cluster and, using the virial theorem, calculated the mass of the cluster. The number he obtained exceeded the expected value from the luminosity of the cluster considerably. He called the additional mass *dark matter* (*dunkle Materie* in German), being one of the first to use this terminology. [3]

One of the most prominent and comprehensible example of evidence for dark matter is the study of rotation curves of spiral galaxies. By measuring the velocity and equating the gravitational and the centrifugal force for visible stars and gas, one can deduce the mass distribution along the distance from the center of the galaxy. The result is that the gravitational mass distribution does not match the visible distribution of matter especially for large radii, where the rotation velocity still stays constant, although the density of visible matter is very small [4, 5, 6]. Figure 1.1 shows an example of such a rotation curve.

Other methods to determine the mass of galaxies and galaxy clusters, such as gravitational lensing (e.g. [7]), as well as the existence of hot gas

---

[1]Even before Zwicky, in 1932 Jan Hendrik Oort analyzed the vertical velocity of stars near the galactic plane in and concluded the existence of additional matter [1]. However, his calculations and conclusions later turned out to be incorrect and are not considered evidence for dark matter anymore [2].

in clusters that would not be bound by the gravitational potential of visible matter alone, confirm the conclusion that there is additional invisible mass.

Attempts have been made to explain these phenomena without the presence of dark matter, by arguing that Newton's laws of motion and general relativity could be altered on very large scale (*Modified Newtonian Dynamics – MOND*) [8].

However, observations on 1E 0657558 (*Bullet Cluster*) support the dark matter hypothesis over MOND: Two galaxy cluster collided around 100 million years ago and while X-ray emissions show that the intergalactic gas of the two clusters were clearly slowed down, gravitational lensing reveals that most of the mass in both clusters was virtually unaffected by the collision and passed through each other, indicating that the vast majority of the mass in the clusters consists of something different than intergalactic gas. [9]

Another explanation for dark matter that doesn't introduce new particles are Massive Astronomical Compact Halo Objects (MACHOs), such as black holes, neutron stars, or brown or white dwarfs, that to explain the gravitational phenomena should make up most of the mass in galaxies especially in areas far from the center. However, gravitational lensing allows to search for them specifically and shows that the number of MACHOs is not high enough to make dark matter unnecessary. Also, these astronomical objects should not have existed before the structure formation in the early universe[2]. However, models to explain the fluctuations in the cosmic microwave background (CMB) need dark matter that existed already then, to fit real-world observations:

The CMB was produced when radiation decoupled from matter at a temperature of around $3000\,\mathrm{K}$ and the universe thus became transparent for photons. Due to the expansion of the universe, the temperature today is around $2.7\,\mathrm{K}$. Fluctuations in the order of around $60\,\mu\mathrm{K}$ are observed, that can be retraced to density fluctuations in the early universe. These density fluctuations are too small to be compatible with the structure formation in the universe with baryonic matter alone. Non-baryonic cold non-relativistic dark matter is required that didn't interact with the photons when the CMB decoupled, but still supported the structure formation gravitationally. [11]

---

[2]Primordial black holes formed before the nucleosynthesis have been suggested as a possibility, but there are also several constraints. See [10] for details.
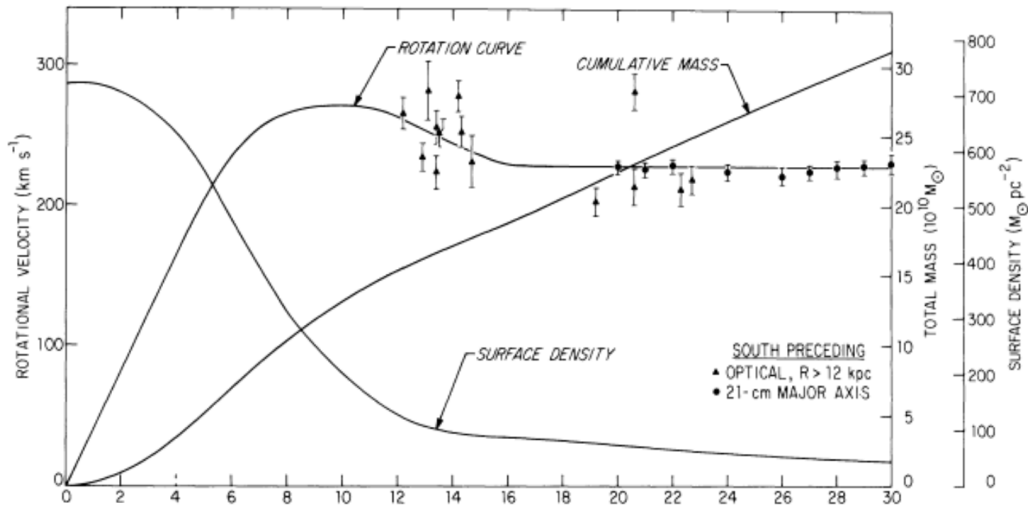
Figure 1.1: Rotation curve of the Andromeda Galaxy [14].

In the *Millennium Run* the structure formation with cold, non-relativistic dark matter was famously and successfully simulated, proving that the assumptions made were consistent with real-world observations. [12]

The Big Bang nucleosynthesis gives another indication for the existence of dark matter already in the early universe: The density of baryons that follows from the nucleosynthesis and the distribution of the elements is not consistent with measurements of the mass density in the universe. The difference must thus be made out of another type of matter. [13]

1.2 Dark Matter Models

In spite of the evidence for dark matter, little is known about its actual particle properties. The properties that follow from the evidence in section 1.1 are that they should not interact electromagnetically, move with non-relativistic velocities, be stable and massive. None of the known particles in the standard model fulfill these properties. Even though neutrinos do not interact electromagnetically and are stable, their mass is too low ($m_\nu <$ 1.1 eV [15]) to be non-relativistic cold dark matter. Therefore physics beyond the standard model has to be considered.

1.2.1 WIMPs

Weakly Interacting Massive Particles (WIMPs) are hypothetical dark matter particles with a mass in the range of $10\,\mathrm{GeV}$ to $100\,\mathrm{TeV}$ (often a mass around the weak scale $100-1000\,\mathrm{GeV}$ is assumed). Weakly interacting means in this case, that it couples directly to the W and Z bosons. This implies that their annihilation cross section is just around the cross section required for the observed amount of dark matter to be produced thermally during the early stages of the universe, $\langle\sigma(\chi\chi \to X)v\rangle \approx 3 \cdot 10^{-26}\,\mathrm{cm^3 s^{-1}}$. This seeming coincidence is often called the WIMP miracle and is seen as a strong indication for WIMPs as predominant dark matter component. [16]

Supersymmetry

A popular extension of the standard model is Supersymmetry (SUSY). The concept is that every standard model particle has a supersymmetric partner particle with a spin different by $1/2$. As an additional quantum number, R parity is introduced. Standard model particles have the R parity $+1$ and their supersymmetric partners -1. SUSY could explain why the Higgs boson is relatively light, as the mass term from each particle would be canceled out by its supersymmetric partner. Also, introducing the SUSY particles would make unifying the strong and the electroweak force at high energies possible. If R parity is conserved, the lightest supersymmetric particle would be stable and is often predicted to be the neutralino, an electrically neutral and weakly interacting massive fermion. [17]

Kaluza-Klein Particles

In the 1920s Theodor Kaluza and Oskar Klein tried to unify gravitation and electromagnetism, introducing an extra spatial dimension. The idea of extra dimensions is still discussed in theoretical physics and also includes the prediction of new KK particles of which the lightest, similar to SUSY introducing a new symmetry, would be stable. This lightest KK particle (LKP) is predicted to be a spin-1 WIMP with a mass in the TeV region. [18]

Other WIMPs

The SUSY neutralino and the LKP are only two examples of WIMP candidates. For other theories, see for example [19], [20], [21], [22] or [23].

1.2.2 Axions

The axion was postulated to solve the strong CP problem: QCD (quantum chromodynamics) seems to preserve CP symmetry, the combination of conjugation (C) and parity (P). Although within QCD, there is no reason why CP violation is forbidden, no such violation is observed. More precisely, the angle θ describing the CP violation could take any value between 0 and 2π, but seems to be exactly 0. Peccei and Quinn offered a solution in 1977 [24], introducing a symmetry that would fix θ to zero. This theory would then also predict a new particle, the axion, which could then also be a dark matter candidate. [25]

1.2.3 Sterile Neutrinos

Neutrinos that do not interact weakly are called sterile. Their existence could solve observed abnormalities in accelerator and reactor neutrino experiments and also be a dark matter candidate. However, their small interaction cross section would make them hard to detect. [26]

1.2.4 Hidden Dark Matter

Weak interaction is allowed for dark matter, but it could also be that dark matter only interacts gravitationally with baryonic matter, which would make its discovery much more difficult, or via unknown non-standard-model interactions. A consequence of this so-called hidden dark matter would be that the dark matter coupling g_X isn't necessarily the same as the weak coupling g_{weak}. The WIMP miracle (section 1.2.1) was that the combination of the weak coupling and a dark matter mass (the factor $\frac{m_{\text{weak}}^2}{g_{\text{weak}}^4}$) naturally yields the correct annihilation cross section and the correct dark matter density. If however the dark matter coupling wasn't fixed as the weak coupling, the same miracle could happen for completely different dark matter masses (WIMPless miracle). [17]

1.2.5 Conclusions

The discussed examples are only a fraction of the most popular present dark matter theories. All of these theories are motivated otherwise than dark matter, but predict particles that could at the same time elegantly solve

the dark matter problem. However, elegance does not necessarily mean that the theory is also implemented in reality. All of the actual evidence for dark matter is gravitational, besides that little is known about its actual properties. Specifically the hidden dark matter theories allow for a broad range of dark matter masses and different types of interactions, meaning that experimentally it should be tried to approach the dark matter search with as little prejudice as possible.

1.3 Direct Dark Matter Detection

Generally, if there is any kind of interaction between dark matter and standard model particles, there are three ways to access this interaction: By producing dark matter by colliding standard model particles, by searching for decay products of annihilating dark matter particles, or by searching for signals of dark matter particles scattering off standard model particles. The third way is called direct detection. The technical challenges in this method lie especially in the low cross section and thus interaction rate, compared to the amount of background, but also the low recoil energies.

The electron mass is around $0.5 \, \mathrm{MeV/c^2}$, while the proton and neutron masses are around $1 \, \mathrm{GeV/c^2}$ [27]. This means that any dark matter particle with a mass in the range of hundreds of $\mathrm{MeV/c^2}$, or $\mathrm{GeV/c^2}$ or higher, would scatter mainly off nucleons and not off electrons. Typical recoil energies for such cold non-relativistc dark matter elastic scattering off nucleons are expected in the keV range or in the high eV range for low dark matter masses.

Usually two components are expected to be dominant: A coupling to the nuclear spin (spin-dependent, SD) and a scalar coupling (spin-independent, SI). Other possibilities are discussed in this work extensively (especially in chapter 3).

In the spin-independet case, if the scattering amplitudes for scattering off neutrons and protons is identical (which in this case is usually assumed) and can be added up coherently, the overall scattering amplitude simply scales with the number of nucleons in a nucleus, the atomic mass number. The resulting cross-section therefore scales with the squared atomic mass number of the nucleus A.

Under these premises, comparison between different experiments using different target materials is straightforward for spin-independent interaction: The experimentally obtained cross-section, or limits on this cross-section in

the case of null results, can be converted into a dark-matter-nucleon cross section by dividing by A^2.

However, it has to be considered that for larger nuclei and large recoil energies, the assumption of adding up the scattering amplitudes coherently is not entirely valid anymore. This loss of coherence is taken into account by a nuclear form factor $F(q)$, where q is the momentum transfer connected to the recoil energy E_R:

$$E_R = \frac{q^2}{2m_N} \tag{1.1}$$

m_N is the mass of the scattered nucleon (around $1\,\text{GeV/c}^2$). The total cross-section σ for a nucleus is then the cross section for individual nucleons σ_n, scaled with A^2 and the form factor $F(q)$:

$$\sigma = \sigma_n A^2 |F(q)|^2 \tag{1.2}$$

The Helm form factor is based on a simplified semi-phenomenological nuclear model for a nucleus with the spherical Bessel function j_1 and the parameters effective nuclear radius R_1, nuclear skin thickness s and $q = \sqrt{2m_N Q}$ [28, 29]

$$F^2(Q) = \left(\frac{3j_1(qR_1)}{qR_1} \right)^2 e^{-(qs)^2} \tag{1.3}$$

The effect of the form factor for a heavy (tungsten) and a lighter (argon) nucleus and for different dark matter masses is illustrated in figure 1.2. It can be seen that the tungsten (W) is much more affected by the form factor corrections than argon (Ar), and that for a lighter dark matter mass the impact of the form factor is not so clearly visible.

For SD interaction, the dark matter cross section of a nucleus is directly dependent on its spin:

$$\sigma \propto (a_p \langle S_p \rangle + a_n \langle S_n \rangle)^2 \frac{J+1}{J} \tag{1.4}$$

Here J is the total nuclear spin, $\langle S_p \rangle$ and $\langle S_n \rangle$ are the average spin of all protons or neutrons in the nucleus and the factors a_p and a_n scale the strength of the coupling to protons and neutrons. This interaction is obviously only possible, if the target nucleus has nuclear spin.

As the signal for direct dark matter searches is the recoil energy, the velocity distribution plays an important role. There is a maximum velocity
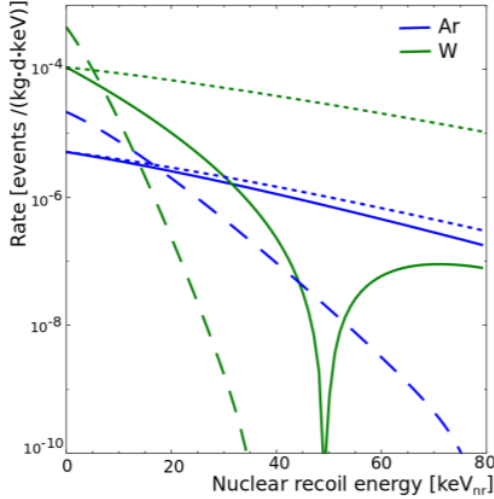
Figure 1.2: SI interaction event rates for tungsten (W) and argon (Ar). The dotted lines show the spectra without the effect of the form factor for a dark matter mass of $100\,\mathrm{GeV/c^2}$, the solid line with the form factor taken into account. The dashed lines show the spectra for a lower mass of $25\,\mathrm{GeV/c^2}$. [30].

for dark matter to stay within the galaxy, which is estimated as around $v_{\mathrm{esc}} \approx 544\,\mathrm{km/s}$ [31, 32]. The shape of the distribution is also an uncertainty. The Standard Halo Model (SHM) [33] assumes a Maxwellian velocity distribution (truncated at v_{esc}) [34]:

$$f(v) = \begin{cases} \frac{1}{N_{\mathrm{esc}}}(\pi v_0^2)^{-3/2} e^{-v^2/v_0^2}, & \text{if } v < v_{\mathrm{esc}} \\ 0, & \text{otherwise,} \end{cases} \tag{1.5}$$

with

$$N_{\mathrm{esc}} = \mathrm{erf}(z) - \frac{2}{\sqrt{\pi}} z e^{-z^2} \tag{1.6}$$

and $z = \frac{v_{\mathrm{esc}}}{v_0}$. v_0 is here the most probable velocity, which is the velocity of the sun relative to the center of our galaxy, $v_0 \approx 220\,\mathrm{km/s}$.

Additionally, the earth orbiting the sun contributes to the relative velocity between the target and dark matter. As this modulation is relatively small, over the course of a year this contribution almost completely averages out. However, there is a difference in the energy spectrum during the

16

year. Specifically, there is an expected shift towards higher velocities and thus higher recoil energies in summer, resulting also in an increase of the total event rate, as more particles exceed the energy threshold of a detector. Although the generally low rates make it difficult to detect this effect, some experiments use it as a possible signal signature.

As of today, there is no conclusive hint for a dark matter signal in direct experiments. Experiments regularily publish limits on the dark-matter-nucleon cross sections. Most experiments are designed with spin-independent interaction (and some with spin-dependent) in mind and the efforts are correspondingly optimized to cover as much parameter space as possible. In the case of SI scattering, this can mean choosing target materials with high nuclear mass numbers A, as the strength of the interaction scales with A^2. However, lighter targets have the advantage that their dark matter recoil spectrum extends to higher recoil energies.

An important points to consider is background reduction. As dark matter events are so rare, the signal is dominated by a large amount of background events from different kinds of radiation. To reduce the flux of cosmic rays, all major direct dark matter experiments are set up in underground labotaries and are equipped with additional shielding. Especially muons can create secondary particles that resemble the dark matter signal. Also, materials around the detector have to be chosen very carefully to avoid radioactive contamination.

Most background radiation causes electronic recoils, whereas the dark matter signal even for masses below $1\,\mathrm{GeV/c^2}$ are expected as nuclear recoils. Therefore most experiments try to distinguish electronic and nuclear recoils for further background reduction. As most signal events have a low recoil energy (as shown in figure 1.2), another focus for experiments is a low energy thresholds. This becomes even more important for lower dark matter masses, as the recoil spectra get steeper.

There is a large number of former and active dark matter experiments today. The most sensitive experiments for higher dark matter masses are large xenon experiments, such as XENON1T [35], LUX [36] or PandaX [37]. The xenon nucleus is relatively large (with a standard atomic weight of 131.3) and the mass of the target in the case of XENON1T even exceeds a ton. The CRESST experiment only has a small fraction of this target mass and is therefore much less sensitive for higher ($\gtrsim 5\,\mathrm{GeV/c^2}$) dark matter masses. For low dark matter masses ($\lesssim 2\,\mathrm{GeV/c^2}$) however, a low energy threshold

becomes more important than a large target mass and large target nuclei. In this region CRESST is currently the most sensitive dark matter experiment.

The CRESST experiment is described in more detail in the following chapter.

Chapter 2

The CRESST Experiment

The CRESST collaboration consists of groups from Italy, Austria and Germany. Currently (since 2016) the third stage of the experiment, called 'CRESST-III', is running. The name *CRESST* stands for Cryogenic Rare Event Search with Superconducting Thermometers. 'Rare Events' refers to dark matter signals, 'Superconducting Thermometers' to transition edge sensors that are used for read-out. The system has to be kept at a low temperature, hence 'Cryogenic'. The experiment is set up in one of the largest underground labotary of the world, the Laboratori Nazional del Gran Sasso (LNGS) in the Abruzzo region in Italy. Around 1400 m of rock (3600 m water-equivalent) of the Gran Sasso mountains above the laboratory halls shield this and other experiments from cosmic rays.

Around the CRESST detectors, additional shielding out of (from outside to inside) polyethylene, lead and copper and again polyethylene is installed. The reason for this setup is that lead and copper shield γ-rays and the outer polyethylene shields external neutrons. The inner additional polyethylene shield is against neutrons that can be produced in the lead or copper. It is particularly important to shield against neutrons, as they produce nuclear recoils in the energy region where dark matter signals are expected and thus can mimic these signals. Cosmic muons can also produce neutrons. Underground, the muon flux is already reduced by multiple orders of magnitude. Additionally, an active muon veto is installed around the experiment. Figure 2.1 shows a schematic drawing of the setup.

To achieve the required low temperature of around $5\,\mathrm{mK}$, a $^3\mathrm{He}/^4\mathrm{He}$ dilution refrigerator is used. The cooling system needs to be refilled with liquid nitrogen and liquid helium three times per week.
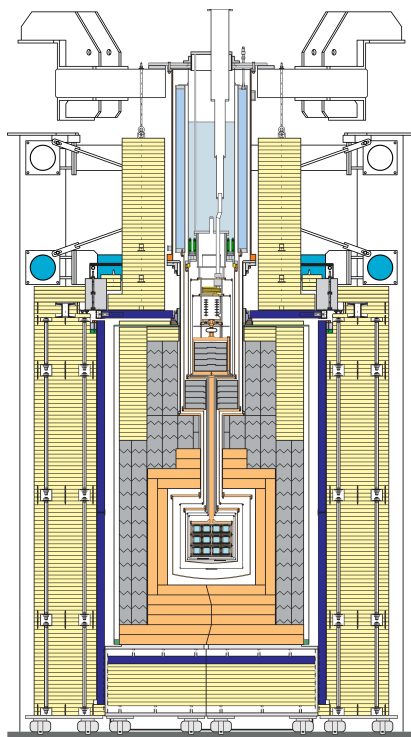
Figure 2.1: Drawing of the CRESST setup. The carousel with the actual detectors can be seen in the center of the picture. The yellow shielding is polyethylene, gray is lead and orange is copper. In dark blue the muon veto is shown. On top of the setup sits the cryostat. [38]

2.1 Detectors

The CRESST detectors consist of a phonon detector and a separate light detector. The current phonon detectors are $CaWO_4$ crystals, but the design of the experiment also allows to use different target materials, or to use multiple materials at the same time. The scintillating crystals produce simultaneous heat (phonon) and light signals. This allows discrimination between electronic and nuclear recoils, because electronic recoils produce more light for the same recoil energy. As the expected dark matter signals are nuclear recoils, but most of the background is electron recoils, this reduces the background of events that resemble dark matter signals significantly. For

energy reconstruction, only the phonon signal, which to a large degree is independent of the particle type, is used.

The mass of CRESST-III $CaWO_4$ crystal is around $24\,g$ and its size is $(20 \times 20 \times 10)\,mm^3$. In former phases, more massive detectors were used. For example, the detector from CRESST-II with the lowest threshold, 'Lise', was around $300\,g$.

Attached to the crystal is the silicon-on-sapphire light detector. Both the phonon detector (main crystal) and the light detector are equipped with separate transition edge sensors (TES). The detector is held in place by sticks also made out of $CaWO_4$ and also equipped with TES in order to be able to distinguish and veto events that don't occur in the main absorber, but in the sticks. The whole detector is enclosed by a scintillating and reflecting foil.

2.2 Data Read Out

The basic principle of the cryogenic detectors is that the energy that incoming particles deposit, creates phonons that are collected in a thermometer which can be read out digitally. The thermometers used are the aforementioned TES. They are made out of tungsten and operated at the transition temperature (around $15\,mK$) between superconductivity and normal conductivity. A small energy and with it a small temperature increase leads to a change in their resistance. The TES is connected in parallel with a coil in a circuit with a constant bias current. The resistance change of the TES changes the current going through the coil and thus a change in magnetic flux, which is measured precisely by a super-conducting quantum interference device (SQUID).

The sampling rate of the system is $25\,kS/s$. The data are filtered offline with the so-called optimum filter. This filter compares the Fourier transformed pulse to that of noise on the one hand and averaged noise-free standard events on the other hand. With this method, even small pulses can be discriminated from noise, which improves both the energy threshold and the energy resolution.

2.3 Energy Calibration and Bands

There are many detours of the initial energy deposit, to a temperature increase in the TES, to a resistance change, to a current change, to a change of magnetic flux, to the output signal of the SQUID and finally to a digitized signal. This makes it impossible to directly trace the strength of the signal back to the original recoil energy. Instead, calibration with radioactive sources that deposit well-known energies has to be carried out.

During former CRESST phases, a ^{57}Co source was used that emitted photons with an energy of 122 keV. However, the behaviour of the signal with respect to its deposited energy is not entirely linear, espacially for higher energies. With improving sensitivity in CRESST-III, at 122 keV the point of non-linearity was already reached. Therefore, the L1 peak at 11.27 keV that originates from cosmogenic activation of ^{182}W is used for calibration.

The height of a pulse is used to scale an event and determine its deposited energy. Up until CRESST-II, every pulse was fitted with a standard event. A standard event is the average over many typical pulses and gives a noise-free templated for the fit. There are multiple free parameters in the fit, with the pulse height being one of them. For higher energies, when the pulse height does not grow linearly with the energy deposit anymore due to saturation effects, the energy can still be reconstructed by truncating the pulse, i.e. only using the lower part of a pulse, where the behaviour is still linear.

For CRESST-III, the output of the optimum filter is used to determine the pulse height with more precision. The treatment of the non-linearity however becomes more complicated and is handled with a combination of the optimum filter and the truncated standard event fit. At least for recoil energies below 16 keV, this procedure works well. For this reason, and as the focus of the CRESST experiment is light dark matter and low recoil energies, only recoil energies below 16 keV are taken account for the CRESST-III dataset published in 2019 [39].

Under the assumption that the large part of the energy is deposited in the phonon detector, only the phonon detector is used to determine the recoil energy. A γ line is used for energy calibration. As γs deposit a larger fraction of their energy in the light detector than nuclear recoils, the recoil energy for nuclear recoils tends to be overestimated with this method. When the expected signal spectrum raises towards lower energy, as it is the case for the standard SI interaction, this leads to conservative limits and thus does not pose a problem. Strictly speaking, this is not always true when investigating

more exotic spectral shapes, as in chapter 3. However, this effect is small (in the order of a few percents, depending on the scintillation light efficiency of the crystal [40]) and is thus neglected in this work.

In addition to the energy, the light yield is the second important parameter of an event. The light yield is defined as the ratio of the deposited energy in the light detector to the energy in the phonon detector, normalized to the ratio produced by electron recoils. This means that for electron recoils, the average light yield is defined as 1 and for nuclear recoils smaller (close to 0). The expected light yield (quenching factors) for the different target nuclei were determined in [41].

To calibrate and fit the bands of nuclear recoils (i.e. the light yield region in which nuclear recoils of certain energies fall), prior to actual measurements the detectors are operated with an active neutron source, allowing a larger database of nuclear recoils, which are rare by design in background datasets. Figure 2.2 shows the result of the neutron calibration and the fitted recoil bands.

Especially for low energy nuclear recoil events where the expected light signal is very close to zero, the noise can dominate the very small signal, which can lead to a reconstructed negative pulse height and thus a negative light yield. This has no special meaning, but is only a consequence of measurement inaccurancies and statistical effects. The same fluctuations in the opposite directions lead to high light yields for low recoil energies even for nuclear recoils (see the shape of the bands in figure 2.2).

2.4   Data Selection

It sometimes happens that detectors record faulty data that don't allow a correct energy reconstruction. Twenty percent of the recorded data are randomly chosen as training data, and the remaining eighty percent is kept as the actual blind dataset, meaning that, in order to avoid bias, the dataset that is actually used for the final analysis was not looked at beforehand. All prior investigations, tests of the analysis methods and definitions of methods to discard erroneous data were only performed on the training dataset. Additional to the training data that is discarded prior to the final analysis, there are certain criteria to discard events or entire periods of data taking.

The rate cut removes periods where the overall trigger rate is significantly higher. As the normal background rate should not be enhanced for certain
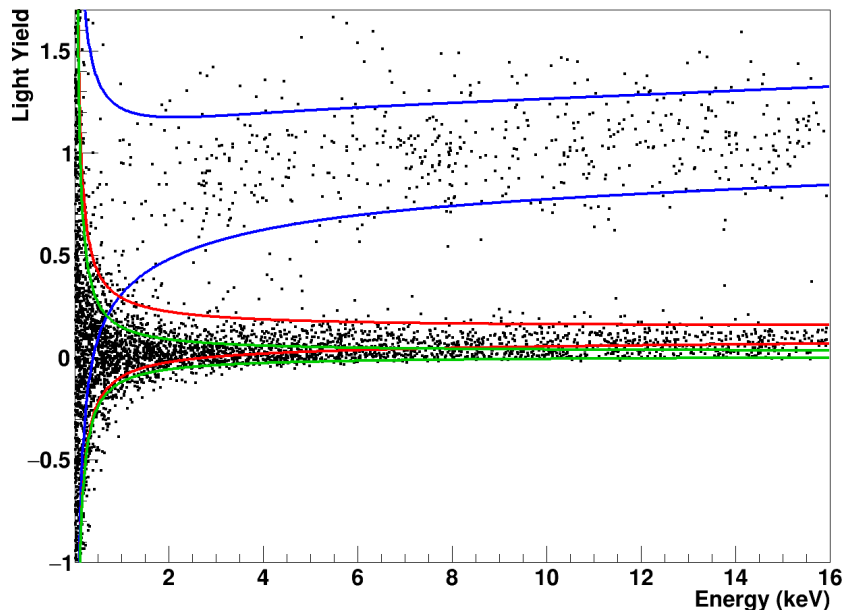
Figure 2.2: Neutron calibration data for detector A of CRESST-III. Black dots are events, the blue line is the fitted β/γ band (i.e. electron recoils), in red the band for oxygen and in green the band for tungsten nuclear recoils. The calcium band (between oxygen and tungsten) is not shown for reasons of clarity. [38]

time periods, this is caused by either external disruptions or disturbances in the electronics.

It is important that the detectors are always at the same operating point in the transition curve. To ensure this, heater control pulses are injected to the sensors and depending on the measured feedback, the heating power is adjusted. If these control pulse heights are significantly different to their usual values, the corresponding time periods are also removed from the data (stability cut).

There is also a cut that removes events where the pulse shape is different to normal events. This is again done with the standard event fit: When the root mean square (RMS) difference between the actual and the fitted pulse is too large, the event is removed (RMS cut).

Then, events that occured not only in the main crystal, but also in the holding sticks, are discarded. Events that actually occur in the stick but also depose some energy in the main crystal without a corresponding light signal

can mimic nuclear recoils. Events with a light signal, but where the corresponding phonon signal did not exceed the trigger threshold are also removed. Their reconstructed energy would lie below the actual energy threshold.

Events in the detectors that coincide with events in the muon veto are also removed. Muons can potentially produce neutrons inside the shielding of the experiment. Also to minimize neutron induced events, events that occur in multiple detectors simultanously are discarded, because neutrons can deposit energy in multiple detectors, whereas for dark matter with its low cross section this is extremely unlikely.

In total, as an example for detector A in CRESST-III, 65% of events in the signal region survive after all cuts. [40]

2.5   Trigger Threshold

Lowering the trigger threshold is a priority for CRESST. As described in section 1.3, for low mass dark matter particles, the energy spectrum becomes more steep, which means that most of the events occur at very low recoil energies. For higher dark matter masses, the loss of events at low recoil energies can be compensated with a higher target mass, as it is done by the large xenon experiments (e.g. XENON1T, LUX or PandaX). For lower masses, this is not possible anymore when the majority of events fall below the energy threshold.

In order to analyze the data, it is also important to know the value of the energy threshold and the survival probability of events in dependence of their energy. The trigger threshold itself should be set to the point from which on actual events can be distinguished from noise. A lower trigger threshold allows more actual events to pass and thus to be more sensitive especially to low mass dark matter, however it also happens more often that the noise triggers by itself, for higher trigger thresholds noise triggers happen less, but sensitivity for actual events gets lost. As a compromise, the trigger threshold is set to the point so that noise triggers happen in average once per kg target mass and day of data taking.

For detector A of CRESST-III, this trigger threshold is 30.1 eV, for Lise, the phonon detector with the lowest energy threshold of CRESST-II, the energy threshold was 311 eV.

The actual energy threshold is not a sharp value, but in the region of the threshold, the signal survival probability rises with increasing energy. It

is mathematically described by an error function around the specified value, with a width of around $5.3\,\mathrm{eV}$ for detector A and $91\,\mathrm{eV}$ for Lise.

2.6   Energy Spectrum

Figure 2.3 shows all remaining events after all cuts for detector A recorded between 2016 and 2018. The bands are the same as in figure 2.2. The acceptance region is defined between the energy threshold ($5.3\,\mathrm{eV}$) and $16\,\mathrm{keV}$ in the energy, and between the mean of the oxygen band and the 99.5 % lower boundary of the tungsten band in the light yield. The reason for this definition is that in the upper half (in terms of light yield) of the nuclear recoil bands, there is a large overlap from the β/γ band. Therefore only the lower half is used. The oxygen band is the band with the highest light yield out of the nuclear recoil bands. When chosing the mean of this band as the upper limit of the acceptance region, it is therefore assured that statistically, a little more than 50 % of the nuclear recoil events are below this line. When calculating limits, assuming that half of the events are below the upper bound is therefore a conservative approach. Accordingly, the 99.5 % lower limit is defined with the lowest of the nuclear recoil bands, the tungsten band.

The light yield plot (fig. 2.3) is only used to determine the events in the acceptance region. The final energy spectrum is shown in figure 2.4.

The light yield plot for detector Lise in the previous run is shown in figure 2.5. Here the acceptance region is chosen up to $40\,\mathrm{keV}$. The corresponding energy spectrum is shown and discussed in the context of the effective field theory analysis in section 3.5 (figure 3.1).

2.7   Results

In order to calculate dark matter limits from the energy spectrum, Yellin's optimum interval method is used, which is described in section 3.5. The final limits for spin-independent[1] dark-matter-nucleus interaction compared with other experiments are shown in figure 2.6. It can be seen that the CRESST experiment is leading for dark matter masses below $1.8\,\mathrm{GeV/c^2}$. As discussed in section 1.2, this is well below the mass region where the

---

[1]Recently, within the CRESST collaboration there have been efforts also to provide limits for spin-dependent interaction, using different detectors.
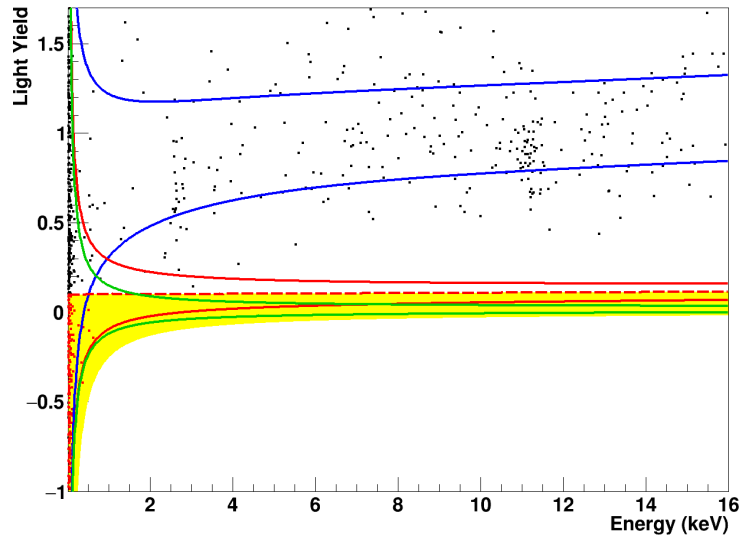
Figure 2.3: Light yield and energy of events for run 34 in detector A. In blue the β/γ band is shown, in red the oxygen and in green the tungsten band. The yellow area is the acceptance region. [38]

WIMP is expected. The CRESST experiment is thus naturally focussed on more exotic dark matter. It can thus be argued, that the simplifications made when assuming a scalar-only interaction are not well-founded. An alternative framework how CRESST data could be analyzed is discussed in more detail in the following chapter.
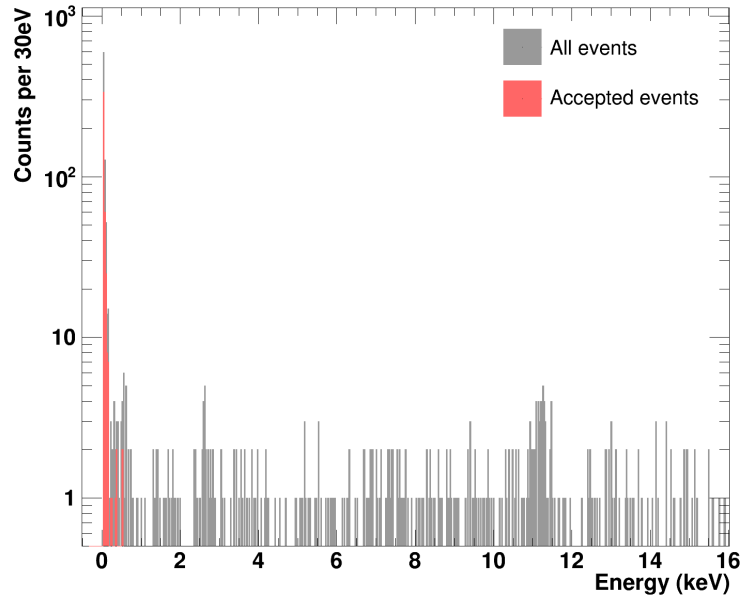
Figure 2.4: Energy spectrum of all events for run 34 in detector A. Events in the acceptance region are highlighted in red.[38]
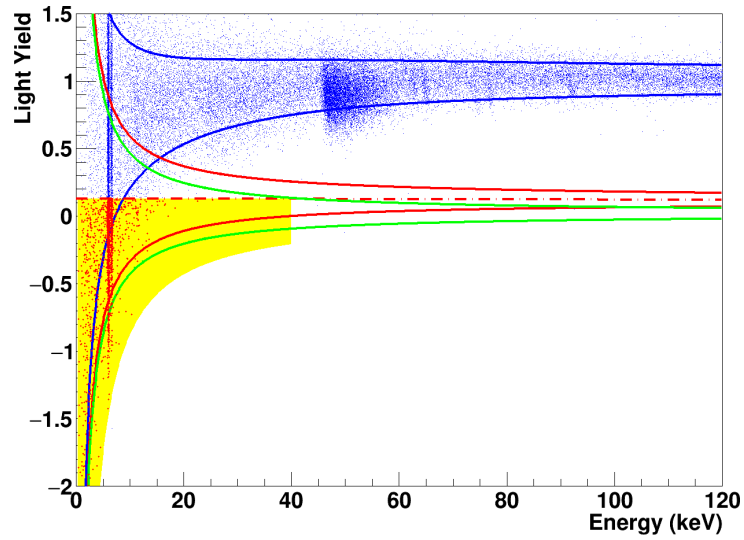
Figure 2.5: Light yield and energy of events for run 33 in detector Lise. In blue the β/γ band is shown, in red the oxygen and in green the tungsten band. The yellow area is the acceptance region. [38]

Figure 2.6: 90 % confidence limits on the dark matter particle-nucleon cross section for elastic, spin-independent interaction for light dark matter ($< 10\,\mathrm{GeV/c^2}$) by different experiments. CRESST results are shown in red. [38]

Chapter 3

Effective Field Theory Analysis of CRESST Data

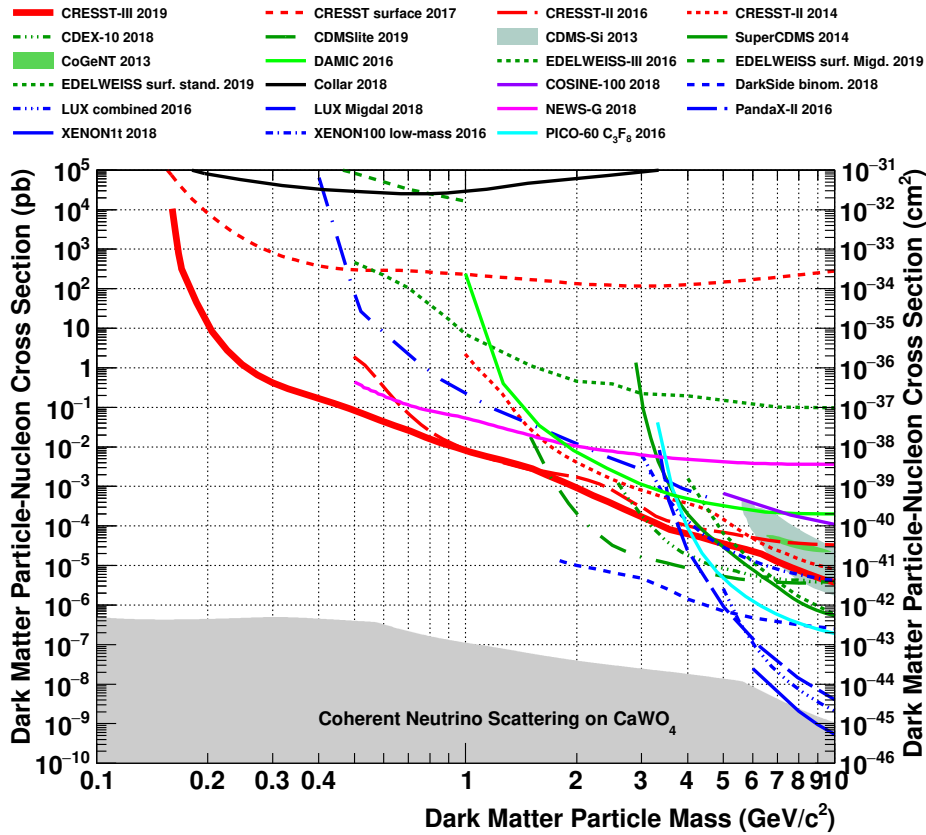## 3.1 Introduction

Whenever new, improved limits are published by a dark-matter experiment collaboration, two general purposes are served. The first is to constrain parameter space, which helps to enhance the knowledge on dark matter properties. The second purpose is the comparison between experiments in regards to dark matter discovery. Dark matter experiments are generally designed with the ultimate goal of detecting dark matter and not only constraining parameter space. By publishing limits that cover previously unconstrained parameter space, the experiment proves its sensitivity and this is generally interpreted as its potential to be the first experiement to detect dark matter, should its real-world properties be in the given experiment's favor.

However, each of the two purposes is only served under certain conditions. These assumptions are reasonably motivated, but partly only driven by simplicity and minimalism. In particular, it is usually assumed that dark matter interacts with the target nucleus via an elastic contact interaction scattering with a cross section that is independent of the momentum transfer and either independent (spin independent - SI) or dependent (spin dependent - SD) on the nuclear and dark matter spin (see section 1.3).

Generally, the WIMP (see section 1.2) is seen as the most promising dark matter candidate and assumptions are made with the WIMP in mind. However, today after over 30 years [42] of direct dark matter detection ex-

periments, there is still no conclusive hint on detection. Although there are experiments have produced data that can be interpreted as a dark matter signal [43, 44], other experiments seem to heavily contradict their results under these assumptions (e.g. [35]).

Indirect searches (e.g. [45]) and production analyses with particle collider data (e.g. [46]) have also only yielded in continously improving null results so far. Taking all this into account, it can be argued that the structure of dark matter might be more complicated than originally hoped and assumed.

These considerations have lead to an increasing number of dark matter theories (see also section 1.2), some of them even trying to bring in line the null results with the controversial signal evidence [47, 48]. One approach was that the dark matter particle transitions into a state with a different mass while scattering (*inelastic dark matter*) [49, 50]. Another approach was to not discard momentum dependencies of the interaction. Although under the simplest premises, these interactions are heavily suppressed in comparison to non-momentum dependent interactions, under certain conditions they can become relevant, change the shape of the recoil spectra and also the relative sensitivity of direct detection experiments [51].

From an experimental point of view, instead of probing all of these theory individually (see also section 1.2), it is preferable to analyze the data more globally in a bottom-up approach, without assuming too many dark matter properties beforehand. This particularly also ensures a more straightforward comparison between experiments. An effective field theory (EFT) approach of the dark matter detection is therefore appealing, including all possible operators that can theoretically be relevant in the scattering, without filtering based on models.

The ultimate goal of the following analysis is to set limits on the Wilson coefficients c_i, the parameters that scale the strength of the interaction in the framework of the Effective Field Theory of Dark Matter Detection, with data from CRESST-II detector *Lise* (see chapter 2).[1]

---

[1]When the present analysis was carried out, this was the latest dataset available.

3.2 The Effective Field Theory of Direct Dark Matter Detection

The non-relativistic Effective Field Theory of Direct Dark Matter Detection has been proposed and developed during the last ten years. The idea is to build a theory about the elastic scattering between an unknown dark matter particle and target nucleons, using as little theoretical assumptions as possible. The ideas and principles of the theory are described in detail in [52, 53, 54] and [55].

A first assumption that has to be made is that the momentum transfer in the interaction is small compared to the mediator mass. In this case the mediator can be neglected and the interaction becomes a four-point interaction (similar to the Fermi interaction). Another, related assumption is that the energy scale of the interaction is not high enough for nuclei to become excited. This normally should not pose a problem, as nuclear binding energies are typically of the order $\mathcal{O}(\text{MeV})$, while nuclear recoils from dark matter is of the order $\mathcal{O}(\text{keV})$. Both of these assumptions are also made in the case of standard spin-independent/spin-dependent interaction.

As a starting point, a Hamiltonian density for one-body dark matter-nucleon interaction in the most general form is defined. Under the one-body assumption, the overall Hamiltonian density for a nucleus is just the sum over all A nucleons:

$$\mathcal{H}(\vec{x}) = \sum_{i=1}^{A} \sum_{\tau=0,1} \sum_{k=1}^{15} c_k^\tau \mathcal{O}_k(\vec{x}) t_i^\tau \tag{3.1}$$

t_i^τ for $\tau = 0, 1$ are different isospin states (isoscalar and isovector). c_k^τ are here simple scaling factors. The c_k^τ are allowed to have an isoscalar and an isovector contribution. The latter case means that the interaction can be different for protons and neutrons. The operators $\mathcal{O}_k$ are not defined in this first step, instead they are left as open as possible, but have to be in accordance with several general principles. It is later shown that there are fourteen relevant operators $\mathcal{O}_1$ and $\mathcal{O}_3$ to $\mathcal{O}_{15}$. Therefore the sum over in equation 3.1 goes up to 15. c_2^0 and c_2^1 have to be zero, for $\mathcal{O}_2$ to be not included.

Alternatively, one could define equation 3.1 instead of isoscalar and isovector coupling constants, simply in terms of proton and neutron coupling constants c_k^p and c_k^n:

$$\mathcal{H}(\vec{x}) = 2 \sum_{i=1}^{A} \sum_{k=1}^{15} \left(c_k^p \left(\frac{\mathbb{1} + \tau_3}{2} \right) + c_k^n \left(\frac{\mathbb{1} - \tau_3}{2} \right) \right) \mathcal{O}_k(\vec{x}) \qquad (3.2)$$

Here, τ_3 is the third Pauli matrix in isospin space, causing the components to flip. However, in direct detection experiments, often target nuclei are not sensitive to proton or neutron interactions separately. This is also the case for CRESST, where the most abundant oxygen and calcium isotopes, ^{16}O and ^{40}Ca have the same number of protons and neutrons. Therefore, the formulation of equation 3.1 is more conveniant.

The first principle that has to apply for the operators $\mathcal{O}$ is conservation of momentum, meaning in an elastic scattering that any momentum gained by one particle has to be dispensed by the other. If $\vec{p}$ is the momentum of the dark matter particle before the interaction, $\vec{p'}$ the momentum of the dark matter particle after the interaction, and $\vec{k}$ and $\vec{k'}$ the momenta of the nucleon before and after the interaction, this means for the momentum transfer $\vec{q}$:

$$\vec{q} = \vec{p'} - \vec{p} = \vec{k} - \vec{k'} \qquad (3.3)$$

Also, the interaction has to be independent of the choice of the inertial frame of reference, i.e. has to be Galilean invariant. The momentum transfer is Galilean invariant. Absolute velocities are not Galilean invariant, if the interaction depends on velocities, it therefore has to be the relative velocity difference $\vec{v}$ between the two particles (before the interaction), the dark matter particle χ with velocity $\vec{v}_\chi$ and the nucleon N with velocity $\vec{v}_N$:

$$\vec{v} = \vec{v}_\chi - \vec{v}_N \qquad (3.4)$$

A third obvious constraint on the interaction is energy conservation. In the laboratory frame (the nucleon is initially at rest, $\vec{v}_N = 0$), the non-relativistic kinetic energy before the interaction is the kinetic energy of the incoming dark matter particle, traveling with the velocity $\vec{v}_\chi = \vec{v}$ from equation 3.4:

$$E = \frac{1}{2} m_\chi v^2 \qquad (3.5)$$

After the interaction, the dark matter particle has gained (positive sign by definition of equation 3.3) the momentum $\vec{q}$ and therefore has the velocity:

$$\vec{v}'_\chi = \vec{v} + \vec{q}/m_\chi \tag{3.6}$$

The nucleon has lost the momentum $\vec{q}$ and now has the velocity:

$$\vec{v}'_N = -\vec{q}/m_N \tag{3.7}$$

The total kinetic energy is therefore now:

$$E = \frac{1}{2}m_\chi \left(\vec{v} + \frac{\vec{q}}{m_\chi}\right)^2 + \frac{\vec{q}^2}{2m_N} = \frac{1}{2}m_\chi \vec{v}^2 + \vec{v}\cdot\vec{q} + \frac{\vec{q}^2}{2}\left(\frac{1}{m_\chi} + \frac{1}{m_N}\right) \tag{3.8}$$

Using the reduced mass $\mu_N = \frac{m_N m_\chi}{m_N + m_\chi}$ and comparing to equation 3.5 leads to the following condition:

$$\vec{v}\cdot\vec{q} = -\frac{\vec{q}^2}{2\mu_N} \tag{3.9}$$

In order to have real eigenvalues, the operators of the interaction must also be Hermitian, which means in this case, that exchanging incoming and outgoing states is equivalent to conjugation of the operator. By definition of equation 3.3, the momentum transfer $\vec{q}$ changes its sign when exchanging incoming and outgoing particles. Therefore, $\vec{q}$ itself, which doesn't change sign under conjugation, is not hermitian, but $i\vec{q}$ is. Instead of $i\vec{q}$, depending on the formulation of the theory, often $i\frac{\vec{q}}{m_N}$ is used.

The relative velocity after the interaction is (with equations 3.6 and 3.7):

$$\vec{v}' = \vec{v}'_\chi - \vec{v}'_N = \vec{v} + \vec{q}\left(\frac{1}{m_\chi} + \frac{1}{m_N}\right) = \vec{v} + \frac{\vec{q}}{\mu_N} \tag{3.10}$$

$\vec{v}$ is obviously not Hermitian. From equation 3.9 one can see that the part of the velocity orthogonal to the momentum transfer (meaning $\vec{v}_\perp \cdot \vec{q} = 0$) is:

$$\vec{v}_\perp = \vec{v} + \frac{\vec{q}}{2\mu_N} \tag{3.11}$$

By using equations 3.10 and 3.11, one can proof that $\vec{v}_\perp$ is Hermitian:

$$\vec{v}'_\perp = \vec{v}' + \frac{\vec{q}'}{2\mu_N} = \vec{v} + \frac{\vec{q}}{\mu_N} - \frac{\vec{q}}{2\mu_N} = \vec{v} + \frac{\vec{q}}{2\mu_N} = \vec{v}_\perp \tag{3.12}$$

$\vec{v}_\perp$ also has the property that it is the average of the relative velocity before and after the interaction (see equation 3.10):

$$\vec{v}_\perp = \frac{1}{2}\left(\vec{v} + \vec{v'}\right) = \frac{1}{2}\left(\vec{v}_\chi + \vec{v'}_\chi - \vec{v}_N - \vec{v'}_N\right) \tag{3.13}$$

In summary, the two kinematic, Galilean invariant and Hermitian, quantities that the interaction operators can consist of are $i\frac{\vec{q}}{m_N}$ and $\vec{v}_\perp$. Beside those two, the two other quantities to be considered are the spins of the dark matter particle and the nucleon $\vec{S}_\chi$ and $\vec{S}_N$. They are Galilean invariant and Hermitian by default. Additionally introducing the identity matrix $\mathbb{1}$, all non-relativistic Hamiltonians describing the interaction in this effective field theory are a combination of these five quantities:

$$\mathbb{1}, \ i\frac{\vec{q}}{m_N}, \ \vec{v}_\perp, \ \vec{S}_\chi, \ \vec{S}_N \tag{3.14}$$

Out of these quantities, thirteen operators can be constructed that fulfill the criteria that they are at most linear in $\vec{S}_\chi$, $\vec{S}_N$ and $\vec{v}_\perp$, and at most quadratic in velocities (combinations of $\vec{v}_\perp$ and $i\frac{\vec{q}}{m_N}$). Operators including $i\frac{\vec{q}}{m_N} \cdot \vec{v}_\perp$ do not appear, as this dot product is zero by definition (see equation 3.11). As the non-relativistic theory is effectively an expansion in velocities around zero momentum transfer (and zero relative velocity), operators without velocity dependence are classified as leading order (LO), with linear velocity dependece as next to leading order (NLO) and with quadratic velocity dependence as next to next to leading order (N^{2}LO). As the operators in the end lead to squared matrix elements, a linear velocity dependence actually leads to a quadratic velocity dependence of the cross section, and a quadratic dependence to a dependence of order 4. Theoretically, an infinite number of higher order operators could be constructed, but these are suppressed in this theory. Out of theoretical convention, the list of operators does not include $\mathcal{O}_2 = \vec{v}_\perp^2$ and instead, a fourteenth operator (accordingly called $\mathcal{O}_{15}$) is added to the set, although it is cubic (and therefore N^{3}LO) in velocities (see [55]).

More specifically, the full set of operators that arise in the relativistic description of the dark matter interaction can be retraced to their non-relativistic limit. In the relativistic case, there are 20 possible combinations to form a Lagrangian interaction density out of the six operators $\overline{\chi}\chi$, $\overline{\chi}\gamma^5\chi$, $P^\mu\overline{\chi}\chi$, $P^\mu\overline{\chi}\gamma^5\chi$, $\overline{\chi}i\sigma^{\mu\nu}q_\nu\chi$ and $\overline{\chi}\gamma^\mu\gamma^5\chi$. In their non-relativistic reduction,

these relativistic Lagrangians are all linear combinations of operators of the non-relativistic EFT. However, while $\mathcal{O}_2$ does not appear in any of these linear combinations, operator $\mathcal{O}_{15}$ does appear.[2]

Therefore the following fourteen operators are the foundation of this non-relativistic EFT:

$$\mathcal{O}_1 = \mathbb{1}$$

$$\mathcal{O}_3 = i\vec{S}_N \cdot \left(\frac{\vec{q}}{m_N} \times \vec{v}_\perp \right)$$

$$\mathcal{O}_4 = \vec{S}_\chi \cdot \vec{S}_N$$

$$\mathcal{O}_5 = i\vec{S}_\chi \cdot \left(\frac{\vec{q}}{m_N} \times \vec{v}_\perp \right)$$

$$\mathcal{O}_6 = \left(\vec{S}_\chi \cdot \frac{\vec{q}}{m_N} \right) \left(\vec{S}_N \cdot \frac{\vec{q}}{m_N} \right)$$

$$\mathcal{O}_7 = \vec{S}_N \cdot \vec{v}_\perp$$

$$\mathcal{O}_8 = \vec{S}_\chi \cdot \vec{v}_\perp$$

$$\mathcal{O}_9 = i\vec{S}_\chi \cdot \left(\vec{S}_N \times \frac{\vec{q}}{m_N} \right)$$

$$\mathcal{O}_{10} = i\vec{S}_N \cdot \frac{\vec{q}}{m_N}$$

$$\mathcal{O}_{11} = i\vec{S}_\chi \cdot \frac{\vec{q}}{m_N}$$

$$\mathcal{O}_{12} = i\vec{S}_\chi \cdot \left(\vec{S}_N \times \vec{v}_\perp \right)$$

$$\mathcal{O}_{13} = i \left(\vec{S}_\chi \cdot \vec{v}_\perp \right) \left(\vec{S}_N \cdot \frac{\vec{q}}{m_N} \right)$$

$$\mathcal{O}_{14} = i \left(\vec{S}_\chi \cdot \frac{\vec{q}}{m_N} \right) \left(\vec{S}_N \cdot \vec{v}_\perp \right)$$

$$\mathcal{O}_{15} = - \left(\vec{S}_\chi \cdot \frac{\vec{q}}{m_N} \right) \left(\left(\vec{S}_N \times \vec{v}_\perp \right) \cdot \frac{\vec{q}}{m_N} \right) \tag{3.15}$$

---

[2]The full list of Lagrangian densities, their nonrelativistic reduction and the corresponding linear combinations of nonrelativistic operators can be found for example in [55].

It should be noted how the operators of equation 3.15 behave under transformations. Out of the five quantities (equation 3.14), the identity matrix $\mathbb{1}$ is obviously invariant under all operations. Spins ($\vec{S}_\chi$ and $\vec{S}_N$) and velocities (and momenta) all change signs under time reversal (T), however the complex quantity $i\frac{\vec{q}}{m_N}$ does not. Under parity (P), spins are even, while velocities and momenta change signs.

Therefore, out of the operators from equation 3.15, $\mathcal{O}_1$, $\mathcal{O}_3$, $\mathcal{O}_4$, $\mathcal{O}_5$ and $\mathcal{O}_6$ are T-even and P-even, $\mathcal{O}_7$, $\mathcal{O}_8$ and $\mathcal{O}_9$ are T-even and P-odd, $\mathcal{O}_{10}$, $\mathcal{O}_{11}$, $\mathcal{O}_{12}$ and $\mathcal{O}_{15}$ are T-odd and P-odd, and $\mathcal{O}_{13}$ and $\mathcal{O}_{14}$ are T-odd and P-even.

These symmetry properties are of interest when identifying the nuclear charges and currents of the interaction.

3.3   Nuclear Responses

So far the interaction between a dark matter particle and a nucleon has been considered. $\vec{v}$ describes the relative velocity between these two particles (and $\vec{v}_\perp$ the relative transverse velocity). This velocity is not the same as the relative velocity between the dark matter particle and the target nucleus, as movements of the nucleon inside the nucleus have to be taken into account. The actual relative velocity is the sum of the relative dark-matter-nucleus movement ($\vec{v}^T$) and movements of the nucleon inside the nucleus ($\vec{v}^N$). Correspondingly for $\vec{v}_\perp$:

$$\vec{v}_\perp = \vec{v}_\perp^T + \vec{v}_\perp^N \tag{3.16}$$

$\vec{v}_\perp^T$ is a purely kinematic quantity, whereas $\vec{v}_\perp^N$ is purely nuclear. They both are Galilean invariants and can be treated separately. The intra-nuclear movements depend on the nucleus and are quantified using nuclear response functions. The spin S_N is of course also a purely nuclear property. Only using the nuclear properties, one can identify the nuclear charges[3] $\mathbb{1}$ (vector charge with even P and T symmetry[4]) and $\vec{S}_N \cdot \vec{v}_\perp^N$ (axial charge with odd P and even T symmetry), as well as the currents $\vec{v}_\perp^N$ (convection current with odd P and T), $\vec{S}_N$ (nuclear spin current with even P and odd T), and $\vec{S}_N \times \vec{v}_\perp^N$ (nuclear spin-velocity current with odd P and even T parity).

---

[3]The expressions 'charge' and 'current' are chosen with regards to their (pseudo-)scalar or (pseudo-)vector properties, demonstrating the similarities to standard electroweak nuclear physics, although the actual forces at play could be more exotic.

[4]T symmetry is equivalent to CP symmetry when CPT symmetry is conserved.

The separation in center-of-mass (on nuclear level) and intrinsic components (on nucleon level) can be made for all operators of equation 3.15. At the same time, the macroscopic operators can be related to nuclear operators. For example, the nuclear spin $\vec{S}_N$ corresponds to a sum over all A nucleons of nucleon spin Pauli operators $\vec{\sigma}$ (with a factor 1/2, as nucleons - protons and neutrons - are spin-1/2 particles):

$$\vec{S}_N = \frac{1}{2} \sum_{i=1}^{A} \vec{\sigma}(i) \tag{3.17}$$

Let $\vec{x}_i$ be the position of a single nucleon, then the internal relative velocity operator can be written as:

$$\vec{v}_\perp^N = \frac{1}{2m_N} \left(i \overleftarrow{\nabla} \delta(\vec{x} - \vec{x}_i) - i \delta(\vec{x} - \vec{x}_i) \overrightarrow{\nabla} \right) \tag{3.18}$$

Using these representations (equations 3.17 and 3.18), one can write the Hamiltonian density (equation 3.1 with all the operators from equation 3.15) in a way that intrinsic and external components are completely separated. The external components are condensed in amplitudes l_0^τ, l_{0A}^τ, $\vec{l}_5^\tau$, $\vec{l}_M^\tau$ and $\vec{l}_E^\tau$:

$$\mathcal{H}(\vec{x}) = \sum_{\tau=0,1} \left(\sum_{i=1}^{A} l_0 \tau \delta(\vec{x} - \vec{x}_i) \right.$$

$$+ \sum_{i=1}^{A} l_{0A}^\tau \frac{1}{2m_N} \left(i \overleftarrow{\nabla} \cdot \vec{\sigma}(i) \delta(\vec{x} - \vec{x}_i) - i \delta(\vec{x} - \vec{x}_i) \vec{\sigma}(i) \cdot \overrightarrow{\nabla} \right)$$

$$+ \sum_{i=1}^{A} \vec{l}_M^\tau \cdot \frac{1}{2m_N} \left(i \overleftarrow{\nabla} \delta(\vec{x} - \vec{x}_i) - i \delta(\vec{x} - \vec{x}_i) \overrightarrow{\nabla} \right)$$

$$+ \sum_{i=1}^{A} \vec{l}_5^\tau \cdot \vec{\sigma}(i) \delta(\vec{x} - \vec{x}_i)$$

$$\left. + \sum_{i=1}^{A} \vec{l}_E^\tau \cdot \frac{1}{2m_N} \left(\overleftarrow{\nabla} \times \vec{\sigma}(i) \delta(\vec{x} - \vec{x}_i) + \delta(\vec{x} - \vec{x}_i) \vec{\sigma}(i) \times \overrightarrow{\nabla} \right) \right) t_i^\tau \tag{3.19}$$

This is exactly equation 3.1, only written out and sorted, so that the charges and and currents that were identified before become clear: The vector

charge (first line in equation 3.19), axial charge (second line), convection current (third line), nuclear spin current (fourth line) and nuclear spin-velocity current (fifth line). Explicitly, the external amplitudes are:

$$l_0^\tau = c_1^\tau + i\left(\frac{\vec{q}}{m_N} \times \vec{v}_\perp^T\right) \cdot \vec{S}_\chi c_5^\tau + \vec{v}_\perp^T \cdot \vec{S}_\chi c_8^\tau + i\frac{\vec{q}}{m_N} \cdot \vec{S}_\chi c_{11}^\tau$$

$$l_{0A}^\tau = -\frac{1}{2}\left(c_7^\tau + i\frac{\vec{q}}{m_N} \cdot \vec{S}_\chi c_{14}^\tau\right)$$

$$\vec{l}_M^\tau = i\frac{\vec{q}}{m_N} \times \vec{S}_\chi c_5^\tau - \vec{S}_\chi c_8^\tau$$

$$\vec{l}_5^\tau = \frac{1}{2}\left(i\frac{\vec{q}}{m_N} \times \vec{v}_\perp^T c_3^\tau + \vec{S}_\chi c_4^\tau + \frac{\vec{q}}{m_N}\frac{\vec{q}}{m_N} \cdot \vec{S}_\chi c_6^\tau + \vec{v}_\perp^T c_7^\tau + i\frac{\vec{q}}{m_N} \times \vec{S}_\chi c_9^\tau\right.$$

$$+i\frac{\vec{q}}{m_N}c_{10}^\tau + \vec{v}_\perp^T \times \vec{S}_\chi c_{12}^\tau + i\frac{\vec{q}}{m_N}\vec{v}_\perp^T \cdot \vec{S}_\chi c_{13}^\tau + i\vec{v}_\perp^T\frac{\vec{q}}{m_N}\vec{S}_\chi c_{14}^\tau$$

$$\left.+\frac{\vec{q}}{m_N} \times \vec{v}_\perp^T\frac{\vec{q}}{m_N} \cdot \vec{S}_\chi c_{15}^\tau\right)$$

$$\vec{l}_E^\tau = \frac{1}{2}\left(\frac{\vec{q}}{m_N}c_3^\tau + i\vec{S}_\chi c_{12}^\tau - \frac{\vec{q}}{m_N} \times \vec{S}_\chi c_{13}^\tau - i\frac{\vec{q}}{m_N}\frac{\vec{q}}{m_N} \cdot \vec{S}_\chi c_{15}^\tau\right) \quad (3.20)$$

In this representation it also becomes clear, which operators contribute to which nuclear coupling: Operators $\mathcal{O}_1$, $\mathcal{O}_5$, $\mathcal{O}_8$ and $\mathcal{O}_{11}$ contribute to the vector charge, operators $\mathcal{O}_7$ and $\mathcal{O}_{14}$ to the axial charge, operators $\mathcal{O}_5$ and $\mathcal{O}_8$ to the convection current, operators $\mathcal{O}_3$, $\mathcal{O}_4$, $\mathcal{O}_6$, $\mathcal{O}_7$, $\mathcal{O}_9$, $\mathcal{O}_{10}$, $\mathcal{O}_{12}$, $\mathcal{O}_{13}$, $\mathcal{O}_{14}$ and $\mathcal{O}_{15}$ to the nuclear spin current and operators $\mathcal{O}_3$, $\mathcal{O}_{12}$, $\mathcal{O}_{13}$ and $\mathcal{O}_{15}$ to the nuclear spin-velocity current.

The overall interaction Hamiltonian is the spatial integral over the Hamiltonian density:

$$H = \int \mathcal{H}(\vec{x})\mathrm{d}^3\vec{x} = \sum_{\tau=0,1}\left(\sum_{i=1}^A l_0\tau + \sum_{i=1}^A l_{0A}^\tau\frac{1}{2m_N}\left(i\overleftarrow{\nabla} \cdot \vec{\sigma}(i) - i\vec{\sigma}(i) \cdot \overrightarrow{\nabla}\right)\right.$$

$$+\sum_{i=1}^A \vec{l}_M^\tau \cdot \frac{1}{2m_N}\left(i\overleftarrow{\nabla} - i)\overrightarrow{\nabla}\right) + \sum_{i=1}^A \vec{l}_5^\tau \cdot \vec{\sigma}(i)$$

$$\left.+\sum_{i=1}^A \vec{l}_E^\tau \cdot \frac{1}{2m_N}\left(\overleftarrow{\nabla} \times \vec{\sigma}(i) + \vec{\sigma}(i) \times \overrightarrow{\nabla}\right)\right) t_i^\tau \quad (3.21)$$

40

The initial state of the interaction is described by the momenta of the nucleon $\vec{k}$ and of the dark matter particle $\vec{p}$, the spin quantum numbers of the dark matter particle j_χ and M_χ, as well as by the nuclear spin (J) and isospin (T) quantum numbers J, M_J, T and M_T. As the nucleus is expected to stay in its ground state during the interaction, the nuclear quantum numbers are the same in the final state. The momenta in the final state are $\vec{k'}$ and $\vec{p'}$.

Due to momentum and transverse velocity conservation[5], the matrix elements for the momentum transfer and transverse velocity operator are:

$$\langle \vec{p'}, \vec{k'}, j_\chi, M_\chi, J, M_J, T, M_T | i\vec{q} | \vec{p}, \vec{k}, j_\chi, M_\chi, J, M_J, T, M_T \rangle$$

$$= i\vec{q} e^{-i\vec{q}\cdot\vec{x}} (2\pi)^3 \delta(\vec{k'} + \vec{p'} - \vec{k} - \vec{p}) \tag{3.22}$$

And:

$$\langle \vec{p'}, \vec{k'}, j_\chi, M_\chi, J, M_J, T, M_T | \vec{v}_\perp | \vec{p}, \vec{k}, j_\chi, M_\chi, J, M_J, T, M_T \rangle$$

$$= \vec{v}_\perp e^{-i\vec{q}\cdot\vec{x}} (2\pi)^3 \delta(\vec{k'} + \vec{p'} - \vec{k} - \vec{p}) \tag{3.23}$$

Therefore, for the Hamiltonian H, one can extract the momenta from the states and describe the rest of the interaction with a nuclear matrix element $\mathcal{M}$:

$$\langle \vec{p'}, \vec{k'}, j_\chi, M_\chi, J, M_J, T, M_T | H | \vec{p}, \vec{k}, j_\chi, M_\chi, J, M_J, T, M_T \rangle$$

$$= e^{-i\vec{q}\cdot\vec{x}} (2\pi)^3 \delta(\vec{k'} + \vec{p'} - \vec{k} - \vec{p})$$

$$\times \langle j_\chi, M_\chi, J, M_J, T, M_T | H | j_\chi, M_\chi, J, M_J, T, M_T \rangle$$

$$(2\pi)^3 \delta(\vec{k'} + \vec{p'} - \vec{k} - \vec{p}) i\mathcal{M} \tag{3.24}$$

This matrix element is then according to equation 3.21:

$$i\mathcal{M} = \langle J, M_J, T, M_T | \sum_{\tau=0,1} \left(\langle j_\chi, M_\chi | l_0^\tau | j_\chi, M_\chi \rangle \sum_{i=1}^A e^{-i\vec{q}\cdot\vec{x}_i} \right.$$

$$+ \langle j_\chi, M_\chi | l_{0A}^\tau | j_\chi, M_\chi \rangle \sum_{i=1}^A \frac{1}{2m_N} \left(i\overleftarrow{\nabla}_x \cdot \vec{\sigma}(i) e^{-i\vec{q}\cdot\vec{x}_i} - i e^{-i\vec{q}\cdot\vec{x}_i} \vec{\sigma}(i) \cdot \overrightarrow{\nabla}_x \right)$$

$$+ \langle j_\chi, M_\chi | \vec{l}_5^\tau | j_\chi, M_\chi \rangle \cdot \sum_{i=1}^A \vec{\sigma}(i) e^{-i\vec{q}\cdot\vec{x}_i}$$

---

[5]The transverse velocity was designed so that it is conserved in the interaction, see section 3.2.

$$+\langle j_\chi, M_\chi | \vec{l}_M^\tau | j_\chi, M_\chi \rangle \cdot \sum_{i=1}^{A} \frac{1}{2m_N} \left(i \overleftarrow{\nabla}_x e^{-i\vec{q}\cdot\vec{x}_i} - i e^{-i\vec{q}\cdot\vec{x}_i} \overrightarrow{\nabla}_x \right)$$

$$+\langle j_\chi, M_\chi | \vec{l}_E^\tau | j_\chi, M_\chi \rangle \cdot \sum_{i=1}^{A} \frac{1}{2m_N} \left(\overleftarrow{\nabla}_x \times \vec{\sigma}(i) e^{-i\vec{q}\cdot\vec{x}_i} + e^{-i\vec{q}\cdot\vec{x}_i} \vec{\sigma}(i) \times \overrightarrow{\nabla}_x \right) \Big)$$

$$\times t_i^\tau | J, M_J, T, M_T \rangle \tag{3.25}$$

In the end event rates of experiments are proportional to the squared matrix element, averaged over all spin states. Following equation 3.25, one can write the averaged squared matrix element in the following way:

$$\frac{1}{2j_\chi + 1} \frac{1}{2J + 1} \sum_{\text{spins}} |\mathcal{M}|^2$$

$$= \frac{4\pi}{2J + 1} \sum_{\tau=0,1} \sum_{\tau'=0,1} \left(\left(R_M^{\tau\tau'} W_M^{\tau\tau'}(y) + R_{\Sigma''}^{\tau\tau'} W_{\Sigma''}^{\tau\tau'}(y) + R_{\Sigma'}^{\tau\tau'} W_{\Sigma'}^{\tau\tau'}(y) \right) \right.$$

$$+ \frac{q^2}{m_N^2} \left(R_{\Phi''}^{\tau\tau'} W_{\Phi''}^{\tau\tau'}(y) + \frac{q^2}{m_N^2} R_{\Phi''M}^{\tau\tau'} W_{\Phi''M}^{\tau\tau'}(y) + R_{\Phi'}^{\tau\tau'} W_{\Phi'}^{\tau\tau'}(y) + R_{\Delta}^{\tau\tau'} W_{\Delta}^{\tau\tau'}(y) \right.$$

$$\left. \left. + R_{\Delta\Sigma'}^{\tau\tau'} W_{\Delta\Sigma'}^{\tau\tau'}(y) \right) \right) \tag{3.26}$$

Each of the nuclear charges and currents are bunched together: M corresponding to the vector charge, Ω corresponding to the axial-vector charge, Σ'' and Σ' corresponding to the longitudinal and transverse electric components of the spin current, Δ corresponding to the longitudinal components of the convection current, and Φ'' and Φ' corresponding to the longitudinal and transverse electric components of the spin-velocity current. As the matrix element is squared, also functions as interference between two of these responses appear. The factors W contain all the nuclear properties. The R are factors that are combinations of the matrix elements of the amplitudes $\langle j_\chi, M_\chi | l | j_\chi, M_\chi \rangle$ from equation 3.25:

$$R_M^{\tau\tau'} = c_1^\tau c_1^{\tau'} + \frac{j_\chi(j_\chi + 1)}{3} \left(\frac{q^2}{m_N^2} (v_\perp^T)^2 c_5^\tau c_5^{\tau'} + (v_\perp^T)^2 c_8^\tau c_8^{\tau'} + \frac{q^2}{m_N^2} c_{11}^\tau c_{11}^{\tau'} \right)$$

$$R_{\Phi''}^{\tau\tau'} = \frac{q^2}{4m_N^2} c_3^\tau c_3^{\tau'} + \frac{j_\chi(j_\chi + 1)}{12} \left(c_{12}^\tau - \frac{q^2}{m_N^2} c_{15}^\tau \right) \left(c_{12}^{\tau'} - \frac{q^2}{m_N^2} c_{15}^{\tau'} \right)$$

$$R_{\Phi''M}^{\tau\tau'} = c_3^\tau c_1^{\tau'} + \frac{j_\chi(j_\chi + 1)}{3}\left(c_{12}^\tau - \frac{q^2}{m_N^2}c_{15}^\tau\right)c_{11}^{\tau'}$$

$$R_{\Phi'}^{\tau\tau'} = \frac{j_\chi(j_\chi + 1)}{12}\left(c_{12}^\tau c_{12}^{\tau'} + \frac{q^2}{m_N^2}c_{13}^\tau c_{13}^{\tau'}\right)$$

$$R_{\tilde{\Sigma}''}^{\tau\tau'} = \frac{q^2}{4m_N^2}c_{10}^\tau c_{10}^{\tau'} + \frac{j_\chi(j_\chi + 1)}{12}\left(c_4^\tau c_4^{\tau'} + \frac{q^2}{m_N^2}(c_4^\tau c_6^{\tau'} + c_6^\tau c_4^{\tau'}) + \frac{q^4}{m_N^4}c_6^\tau c_6^{\tau'}\right.$$
$$\left. + (v_\perp^T)^2 c_{12}^\tau c_{12}^{\tau'} + \frac{q^2}{m_N^2}(v_\perp^T)^2 c_{13}^\tau c_{13}^{\tau'}\right)$$

$$R_{\tilde{\Sigma}'}^{\tau\tau'} = \frac{1}{8}\left(\frac{q^2}{m_N^2}(v_\perp^T)^2 c_3^\tau c_3^{\tau'} + (v_\perp^T)^2 c_7^\tau c_7^{\tau'}\right) + \frac{j_\chi(j_\chi + 1)}{12}\left(c_4^\tau c_4^{\tau'} + \frac{q^2}{m_N^2}c_9^\tau c_9^{\tau'}\right.$$
$$+ \frac{(v_\perp^T)^2}{2}\left(c_{12}^\tau - \frac{q^2}{m_N^2}c_{15}^\tau\right)\left(c_{12}^{\tau'} - \frac{q^2}{m_N^2}c_{15}^{\tau'}\right) + \frac{q^2}{2m_N^2}(v_\perp^T)^2 c_{14}^\tau c_{14}^{\tau'}\right)$$

$$R_\Delta^{\tau\tau'} = \frac{j_\chi(j_\chi + 1)}{3}\left(\frac{q^2}{m_N^2}c_5^\tau c_5^{\tau'} + c_8^\tau c_8^{\tau'}\right)$$

$$R_{\Delta\Sigma'}^{\tau\tau'} = \frac{j_\chi(j_\chi + 1)}{3}\left(c_5^\tau c_4^{\tau'} - c_8^\tau c_9^{\tau'}\right) \tag{3.27}$$

The factors W in equation 3.26 are more complicated to calculate. In order to obtain analytical expressions, a nuclear model has to be assumed. Usually, the responses are calculated numerically using a nuclear shell model code. The procedure is described in detail e.g. in [56].

The CRESST detectors consist of $CaWO_4$. The nuclear response functions W for the most abundant isotopes of oxygen and calcium were calculated and published by Riccardo Catena and Bodo Schwabe in [56]. These nuclear form factors are functions of y, which is a dimensionless parameterization of the momentum transfer q:

$$y \equiv \left(\frac{qb}{2}\right)^2$$

$$b = \sqrt{\frac{41.467}{45A^{-1/3} - 25A^{-2/3}}}\ \mathrm{fm} \tag{3.28}$$

For ^{16}O they obtained:

$$W_M^{00}(y) = 0.000032628e^{-2y}(395.084 - 200.042y + y^2)^2$$

43

$$W_{\Phi''}^{00}(y) = 0.000032628e^{-2y}(3.66055 - y)^2$$

$$W_{M\Phi''}^{00}(y) = e^{-2y}(-0.0471874 + 0.0367831y - 0.00664641y^2 + 0.000032628y^3)$$
$$\text{(3.29)}$$

And for ^{40}Ca:

$$W_M^{00}(y) = 0.000016743e^{-2y}(1378.8 - 1387.54y + 281.953y^2 - y^3)^2$$

$$W_{\Phi''}^{00}(y) = 0.0000376718e^{-2y}(13.117 - 8.74678y + y^2)^2$$

$$W_{M\Phi''}^{00}(y) = e^{-2y}(-0.454214 + 0.759976y - 0.432314y^2 + 0.0971138y^3$$
$$-0.00730079y^4 + 0.0000251146y^5) \qquad \text{(3.30)}$$

For tungsten and other oxygen and calcium isotopes, these nuclear response functions are not available so far. Tungsten is a relatively large nucleus, this makes nuclear shell calculations not only very complicated, but also the applicability of the nuclear shell model for such large nuclei is limited.

Having only nuclear responses available for ^{16}O and ^{40}Ca entails certain limitations: Both of these nuclei have the same number of protons and neutrons, and have spin 0. Therefore they are only sensitive to isoscalar (as indicated by the two zeros W^{00}) contributions to the vector charge (M) and to the longitudinal component of the spin-velocity current. Consequently (cf. equation 3.20), the only contributing operators are $\mathcal{O}_1$, $\mathcal{O}_3$, $\mathcal{O}_5$, $\mathcal{O}_8$, $\mathcal{O}_{11}$, $\mathcal{O}_{12}$ and $\mathcal{O}_{15}$.

As the goal of the analysis is to set limits on the numerical coefficients c_i individually, it is convenient to have form factors not only for the different nuclear responses, but individually for the operators of the form $F_{ij}^{\tau\tau'}$:

$$|\mathcal{M}|^2 \propto \sum_{i,j=1}^{15} \sum_{\tau,\tau'=0,1} c_i^\tau c_j^{\tau'} F_{ij}^{\tau\tau'} \qquad \text{(3.31)}$$

More precisely, it is desirable to define these form factors as follows:

$$\frac{m_T^2}{m_N^2} \sum_{i,j=1}^{15} \sum_{\tau,\tau'=0,1} c_i^\tau c_j^{\tau'} F_{ij}^{\tau\tau'} \equiv \frac{1}{2j_\chi + 1} \frac{1}{2j + 1} \sum_{\text{spins}} |\mathcal{M}|^2 \qquad \text{(3.32)}$$

These form factors can be easily read off by inserting the R from equations 3.27 into equation 3.26, and comparing with equation 3.32. As an example,

in equations 3.27, the product of the coefficients c_1^τ and $c_1^{\tau'}$ only contributes to $R_M^{\tau\tau'}$. Therefore:

$$\frac{m_T^2}{m_N^2}c_1^\tau c_1^{\tau'} F_{11}^{\tau\tau'} = \frac{4\pi}{2J+1}c_1^\tau c_1^{\tau'} W_M^{\tau\tau'}(y)$$

$$\Rightarrow F_{11}^{\tau\tau'}(y) = \frac{m_N^2}{m_T^2}\frac{4\pi}{2J+1}W_M^{\tau\tau'}(y) \tag{3.33}$$

3.4 Spectrum Calculation

3.4.1 General Considerations

In general, the rate R of any interaction of incoming particles with a target is an interaction probability times the rate of the incoming particles. This is equivalent to a cross section σ multiplied by the rate of incoming particles per area. In the case of direct dark matter detecion this is the product of the dark matter velocity v and their particle density, which is the fraction of the mass density ρ_χ and the individual dark matter particle mass m_χ. For a total rate, this has to be summed over all of the N target particles, in this case nuclei:

$$R = \sum_{k=1}^{N}\frac{\rho_\chi}{m_\chi}\langle\sigma_k v\rangle \tag{3.34}$$

As there are different isotopes in the target detector, the cross section σ_k can be different for different nuclei k. The dark matter velocity v is not a distinct value, but follows a distribution $f(v)$. The cross-section is potentially velocity-dependent, it is therefore the average over the product of σ_k and v that goes into the rate calculation, as indicated by the angled brackets $\langle\sigma_k v\rangle$, which in practise is an integral over the velocity distribution:

$$\langle\sigma_k v\rangle = \int \sigma_k f(v)dv \tag{3.35}$$

$$\Rightarrow R = \sum_{k=1}^{N}\frac{\rho_\chi}{m_\chi}\int \sigma_k f(v)dv \tag{3.36}$$

Rather than the total rate, for the comparison with experimental results, one needs an energy spectrum over the recoil energy E_R, i.e. the differential

scattering rate $\frac{\mathrm{d}R}{\mathrm{d}E_R}$. In a non-relativistic elastic collision between a particle 1 with mass m_1 moving with the velocity v_1 and a particle 2 with mass m_2 at rest $v_2 = 0$, from momentum and energy conservation one finds the velocity of particle 2 after the collision $v_2' = \frac{2m_1}{m_1+m_2}v_1 \sin\frac{\theta}{2}$ with the angle of deflection θ, and thus the recoil energy $E_R = \frac{1}{2}m_2 v_2'^2 = \frac{2m_1^2 m_2}{(m_1+m_2)^2}v_1^2 \sin^2\frac{\theta}{2}$. In this case particle 1 is the dark matter particle with mass m_χ and velocity v, and particle 2 is the target nucleus with mass m_T. The reduced mass of the system is $\mu = \frac{m_\chi m_T}{m_\chi+m_T}$ and $\sin^2 x \equiv \frac{1-\cos x}{2}$. The nuclear recoil energy is therefore:

$$E_R = \frac{2m_\chi^2 m_T}{(m_\chi + m_T)^2}v^2 \sin^2\frac{\theta}{2} = \frac{\mu^2}{m_T}v^2(1 - \cos\theta) \tag{3.37}$$

By combining the equations 3.36 and 3.37 and derivating, one obtains the recoil spectrum:

$$\frac{\mathrm{d}R}{\mathrm{d}E_R} = \frac{\rho_\chi m_T}{\mu^2 m_\chi}\sum_{k=1}^{N}\int \frac{1}{v^2}\frac{\mathrm{d}\sigma_k}{\mathrm{d}\cos\theta}f(v)dv \tag{3.38}$$

In the center-of-momentum frame, the differential cross section is related to the matrix elements $\mathcal{M}$ via $\frac{\mathrm{d}\sigma}{\mathrm{d}\cos\theta\mathrm{d}\phi} = \frac{1}{64\pi^2 s}|\mathcal{M}|^2$ for each individual initial and final spin state. In the non-relativistic case, the Mandelstam variable s is simply the squared total mass $s = (m_\chi + m_T)^2$. As there is no dependency on ϕ, the integral over $\mathrm{d}\phi$ gives a factor 2π. Dividing by the number of possible initial dark matter and nuclear spin states ($2j_\chi + 1$ and $2j + 1$ respectively) and summing over all final spins gives:

$$\frac{\mathrm{d}\sigma}{\mathrm{d}\cos\theta} = \frac{1}{2j_\chi + 1}\frac{1}{2j + 1}\sum_{\text{spins}}\frac{1}{32\pi}\frac{|\mathcal{M}|^2}{(m_\chi + m_T)^2} \tag{3.39}$$

The Hamiltonian for the dark-matter-nucleon interaction in the case of the effective field theory is (see section 3.2, equation 3.1):

$$\mathcal{H}(\vec{x}) = \sum_{i=1}^{A}\sum_{\tau=0,1}\sum_{k=1}^{15}c_k^\tau \mathcal{O}_k^i(\vec{x})t_i^\tau \tag{3.40}$$

At the end of section 3.3, form factors $F_{ij}^{\tau\tau'}$ were constructed in such a way that they already contain the sum over the final and the average over the initial spin states, and include a factor m_T^2/m_N^2, as the general strength

46

of an interaction for each target atom scales with the ratio between target nucleus and nucleon mass, which is the number of nucleons in the nucleus, squared (equation 3.32):

$$\frac{m_T^2}{m_N^2} \sum_{i,j=1}^{15} \sum_{\tau,\tau'=0,1} c_i^\tau c_j^{\tau'} F_{ij}^{\tau\tau'} \equiv \frac{1}{2j_\chi + 1} \frac{1}{2j + 1} \sum_{\text{spins}} |\mathcal{M}|^2 \qquad (3.41)$$

With equation 3.39 one obtains:

$$\frac{d\sigma}{d\cos\theta_k} = \frac{1}{32\pi} \frac{1}{(m_\chi + m_T)^2} \frac{m_T^2}{m_N^2} \sum_{i,j=1}^{15} \sum_{\tau,\tau'=0,1} c_i^\tau c_j^{\tau'} F_{ijk}^{\tau'} \qquad (3.42)$$

As before in equations 3.36 to 3.38, the index k stands for the individual target particle, taking into account that the form factor $F_{ijk}^{\tau\tau'}$ is different for every target isotope. Combining this with equation 3.38 leads to the following expression for the recoil spectrum:

$$\frac{dR}{dE_R} = \frac{\rho_\chi m_T}{32\pi m_\chi^3 m_N} \sum_{k=1}^{N} \sum_{i,j=1}^{15} \sum_{\tau,\tau'=0,1} c_i^\tau c_j^{\tau'} \int \frac{1}{v^2} F_{ijk}^{\tau\tau'} f(v) dv \qquad (3.43)$$

Again, similar to the cross section in equation 3.36, the form factors can be velocity dependent and the whole expression $\frac{1}{v} F_{ijk}^{\tau\tau'}$ is therefore averaged over the velocity distribution of incoming particles. In general, the term $c_i^\tau c_j^{\tau'} F_{ijk}^{\tau\tau'}$ allows for interference between different operators and Wilson coefficients. In the case of discovery, the exact shape of the recoil spectrum carries the information on the contribution of combinations or single operators to the interaction between the dark matter and the target particle. However, as dark matter has not been detected yet, this leaves a large parameter space open. Setting only limits for Wilson coefficients of individual operators without interference terms is sufficient to show and compare the performance of different experiments and results in an overseeable number of limits. In equation 3.43 this means that $i = j$ and $\tau = \tau'$.

$$\frac{dR}{dE_R} = \frac{\rho_\chi m_T}{32\pi m_\chi^3 m_N} \sum_{k=1}^{N} \sum_{i=1}^{15} \sum_{\tau=0,1} (c_i^T)^2 \int \frac{1}{v^2} F_{iik}^{TT} f(v) dv \qquad (3.44)$$

The sum over k is a sum over all N nuclei in the target. In practise, the rates are calculated for every isotope separately, and then added up according

47

to the isotopic composition of the target material. If not all isotopes are taken into account, the calculated signal rate is lower.

The calculation of the form factors is described in detail in section 3.3. In the following subsections, the variables of equation 3.44 are discussed, how they are calculated or which value is assumed.

3.4.2   Local Halo Density ρ_χ

The exact value still has a large uncertainty today. Depending on the method of the measurement, values between $\rho_\chi = 0.2\,\text{GeV/c}^2$ and $\rho_\chi = 0.7\,\text{GeV/c}^2$ are estimated [57]. However, this affects all experiments equally and linearly, meaning that the rate can be simply scaled up or down for a different value. In order to assure a comparison, the usual assumed number is $\rho_\chi = 0.3\,\text{GeV/c}^2$.

3.4.3   Target Mass m_T

The target mass is the mass of the detector crystal, which for the module *Lise* from CRESST-II is $m_T = 300\,\text{g}$ (see chapter 2).

3.4.4   Dark Matter Mass m_χ

The dark matter mass is an unknown parameter. For a range of dark matter masses $m_\chi = 0.6 - 100\,\text{GeV/c}^2$, the rate and subsequently a limit are calculated. The final limit plot is therefore a function of the dark matter mass. As CRESST is especially competitive for low dark matter masses, higher masses than $100\,\text{GeV/c}^2$ are not considered.

3.4.5   Nucleon Mass m_N

In reasonable approximation, the mass of a nucleon is one atomic mass unit $m_N \approx 0.9315\,\text{GeV/c}^2$.

3.4.6   Velocity Distribution $f(v)$

For the velocity distribution, the Standard Halo Model is used in this work, which assumes a Maxwellian distribution with the most probable velocity at

$v_0 = 220\,\text{km/s}$ (the rotation velocity of our galaxy at the position of our solar system) and an escape velocity of $v_{\text{esc}} = 544\,\text{km/s}$ (see also section 1.3).

3.4.7 Number of Target Nuclei N and Exposure

The number of molecules N_m can be calculated from the mass m_T and the molar mass M of the material (with the Avogadro constant N_A):

$$N_m = N_A \frac{m_T}{M} \tag{3.45}$$

For *Lise* in CRESST-II, the target material is CaWO$_4$, therefore each of these molecule contains four oxygen and one of each calcium and tungsten atoms. The number of oxygen (N_O), calcium (N_{Ca}) and tungsten (N_W) atoms is accordingly:

$$N_O = 4N_m$$

$$N_{\text{Ca}} = N_m$$

$$N_W = N_m \tag{3.46}$$

The isotopes of these materials appear in their natural isotopic abundance (see table 3.1). For example, if $a_{16\text{O}}$ and $a_{40\text{Ca}}$ are the abundances of ^{16}O and ^{40}Ca, there are $N_{16\text{O}}$ and $N_{40\text{Ca}}$ ^{16}O and ^{40}Ca nuclei in the target detector:

$$N_{16\text{O}} = 4a_{16\text{O}}N_A\frac{m_T}{M}$$

$$N_{40\text{Ca}} = a_{40\text{Ca}}N_A\frac{m_T}{M} \tag{3.47}$$

Using equations 3.45 and 3.47, one can also calculate the mass content for individual isotopes, e.g.:

$$m_{16\text{O}} = 4m_T a\frac{M_{16\text{O}}}{M}$$

$$m_{40\text{Ca}} = m_T a\frac{M_{40\text{Ca}}}{M} \tag{3.48}$$

Calcium has a standard atomic weight of $A_r(\text{Ca}) = 40.08$, tungsten of $A_r(\text{W}) = 183.84$ and oxygen of $A_r(\text{O}) = 16.00$ [59]. Therefore, the molar mass of calcium tungstate is:

$$M = (40.08 + 183.84 + 16.00)\,\text{g/mol} = 239.92\,\text{g/mol} \tag{3.49}$$

Table 3.1: Natural isotopic composition of O, Ca and W [58]

element	Z	A	abundance
O	8	16	0.9976206(9)
		17	0.0003790(9)
		18	0.0020004(5)
Ca	20	40	0.96941(6)
		42	0.00647(3)
		43	0.00135(2)
		44	0.02086(4)
		46	0.00004(1)
		48	0.00187(1)
W	74	180	0.001198(2)
		182	0.264985(49)
		183	0.143136(6)
		184	0.306422(13)
		186	0.284259(62)

To obtain the expected signal energy spectrum for a certain time of measurement, the recoil spectrum (equation 3.44) has to be multiplied with the measurement time. The final spectrum scales linearly with both the target mass and the measurement time, the crucial parameter is therefore the exposure, defined as the product of measuring time T and target mass m_T. The data used for this analysis have an exposure of $m_T \cdot T = 52.15\,\text{kg} \cdot \text{days}$.

Using equation 3.48, the actual effective exposure for the individual isotopes ^{16}O and ^{40}Ca is:

$$m_{^{16}\text{O}} \cdot T = 4 m_T T a \frac{M_{^{16}\text{O}}}{M} = 13.88\,\text{kg} \cdot \text{days}$$

$$m_{^{40}\text{Ca}} \cdot T = m_T T a \frac{M_{^{40}\text{Ca}}}{M} = 8.43\,\text{kg} \cdot \text{days} \qquad (3.50)$$

3.4.8 Wilson Coefficients c_i^τ

The Wilson coefficients c_i^τ are the free parameters of this effective field theory.

3.4.9 Implementation and Spectra

The implementation of the rate calculation is done in MATLAB and is based on the Mathematica package from reference [55] and its MATLAB translation from reference [60].

The dominant (see table 3.1) oxygen and calcium isotopes ^{16}O and ^{40}Ca are the only isotopes taken into account in this analysis, because for the other isotopes, the necessary form factors were not available. This in the end underestimates all modeled spectra. When only setting limits and not reporting discovery of dark matter, this is a valid but conservative approach.

The spectra for ^{16}O and ^{40}Ca are shown in the figures 3.2 and 3.3. As shown in subsection 3.3, both of these elements only have non-zero form factors for isoscalar interaction and the nuclear responses M, Φ'' and $M\Phi''$. As only the following operators have contribution from these responses, only the spectra that these operators cause are shown:

$$\mathcal{O}_1 = \mathbb{1}$$

$$\mathcal{O}_3 = i\vec{S}_N \cdot \left(\frac{\vec{q}}{m_N} \times \vec{v}_\perp \right)$$

$$\mathcal{O}_5 = i\vec{S}_\chi \cdot \left(\frac{\vec{q}}{m_N} \times \vec{v}_\perp \right)$$

$$\mathcal{O}_8 = \vec{S}_\chi \cdot \vec{v}_\perp$$

$$\mathcal{O}_{11} = i\vec{S}_\chi \cdot \frac{\vec{q}}{m_N}$$

$$\mathcal{O}_{12} = i\vec{S}_\chi \cdot \left(\vec{S}_N \times \vec{v}_\perp \right)$$

$$\mathcal{O}_{15} = -\left(\vec{S}_\chi \cdot \frac{\vec{q}}{m_N} \right) \left(\left(\vec{S}_N \times \vec{v}_\perp \right) \cdot \frac{\vec{q}}{m_N} \right) \tag{3.51}$$

The spectra for dark matter masses of $10\,\mathrm{GeV/c^2}$ and $100\,\mathrm{GeV/c^2}$ are compared. The spectral shape is very similar for ^{16}O and ^{40}Ca. Scattering off ^{16}O however can produce slightly higher recoil energies. Comparing the two different dark matter masses $10\,\mathrm{GeV/c^2}$ and $100\,\mathrm{GeV/c^2}$, it can be seen that while for $10\,\mathrm{GeV/c^2}$, nearly the complete energy spectrum is included in the acceptance region for detector Lise up to $40\,\mathrm{keV}$, for $100\,\mathrm{GeV/c^2}$, a large part of energy recoils is above $40\,\mathrm{keV}$ and thus above the upper limit of the acceptance region.

Because of the momentum dependence of operators $\mathcal{O}_3$, $\mathcal{O}_5$, $\mathcal{O}_{11}$, $\mathcal{O}_{12}$ and $\mathcal{O}_{15}$, their spectra do not have their maximum at zero momentum transfer.

The rates in figures 3.2 and 3.3 are shown per kg·days of exposure. For the final spectra to be compared with the real data, these spectra are added up and weighted according to the exposure of the isotopes (equation 3.50).

3.5   Limit Calculation

In a next step, the spectra have to be corrected with regards to how a real detector would record these events, i.e. taking in account the finite energy resolution, cut survival probability and energy threshold (see [61]).

For the energy resolution, they are convoluted with a normal distribution. For detector Lise, the width of this distribution (hence the energy resolution) is $0.062\,\mathrm{keV}$. Then the convoluted function is multiplied with the energy dependent cut survival probability. The numerical function describing this probability was determined before during the analysis. The energy threshold is taken into account by simply setting the modeled spectrum to zero for energies below the energy threshold, which for Lise is conservatively determined as $311\,\mathrm{eV}$.

Finally, the resulting spectrum is compared to the recorded data, which is shown in figure 3.1. There is a large peak visible at around $6\,\mathrm{keV}$, due to an accidental illumination with an X-ray source [62]. When using the optimum interval method, this does not influence the sensitivity significantly.

The idea of the optimum interval method is that when trying to disprove a theory or to set limits, when the background of a signal is unknown or can not be easily modelled, as it is the case with CRESST, one has to exploit certain areas in a spectrum where the recorded spectrum is significantly lower than the modeled spectrum. In the presence of such an unkown background, areas with lots of events do not carry decisive information, as any unknown background could have produced these events. Instead, using Poisson statistics, it is tried to find the area range of the spectrum, where the statistical discrepancy between the modeled and the real spectrum is as significant as possible, in the sense that there is a lack of events in the recorded spectrum. The selection bias of systematically searching for these areas is compensated with a statistical penalty. [63, 64]

The modeled spectra are scaled down as low as possible (by manipulating the Wilson coefficients) so that they still have a discrepancy with the recorded
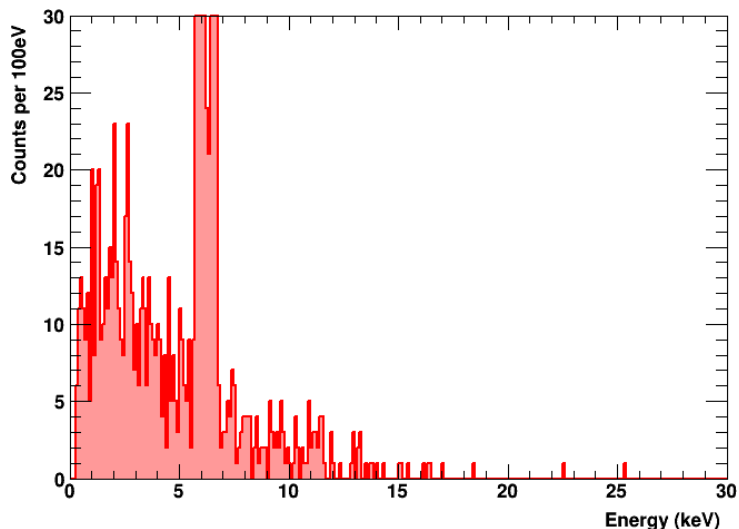
Figure 3.1: Energy spectrum of all accepted events for run 33 in detector Lise. [38]

data of at least 90 % confidence. The whole procedure is repeated for the range of masses between $m_\chi = 0.6 - 100\,\mathrm{GeV/c^2}$ and for the different EFT operators, so that in the end limits on the isoscalar Wilson coefficients c_1^0, c_3^0, c_5^0, c_8^0, c_{11}^0, c_{12}^0 and c_{15}^0 as functions of the dark matter mass are obtained.

3.6 Limits

The final results of this effective field theory analysis are displayed in figures 3.4 and 3.5, compared to results from the CDMS experiment. Similarily to the standard spin-independent limits (figure 2.6), as a consequence of its low energy threshold but low exposure, the strength of the CRESST experiment is in the low mass region. For every of the Wilson coefficients c_1^0, c_3^0, c_5^0, c_8^0, c_{11}^0, c_{12}^0 and c_{15}^0, the most sensitive limits for masses below around $3\,\mathrm{GeV/c^2}$ are set and therefore previously unresearched parameter space was excluded.

A similar analysis was also carried out by the XENON100 collaboration [65]. Their results however are only relevant for higher masses of $10 - 1000\,\mathrm{GeV/c^2}$, well above the area where CRESST is sensitive, and are thus not included in figures 3.4 and 3.5.

53

Each plot shows the dark matter mass on the x-axis and on the y-axis the respective squared Wilson coefficient multiplied by $m_{\text{weak}}^4 = (246.22\,\text{GeV})^4$. All values above the shown limits are excluded with a 90% confidence level. The factor m_{weak}^4 is included to construct a dimensionless variable. The specific value, the vacuum expectation value of the Higgs field, which is related to the Fermi constant and the coupling constant of the weak interaction, is chosen in order to give a scale that is comparable to the weak interaction, although the underlying mechanisms behind the interaction aren't necessarily related to the weak interaction.

The Wilson coefficients are squared, as actually the product of two coefficients (see equation 3.32) goes into the calculation of the squared matrix element and therefore of the interaction rates. However, this analysis was limited to individual (squared) coefficients. In the case of discovery of dark matter, intereference terms between multiple operators will have to be considered when reconstructing the coefficients of the operators from the measured dark matter spectra.

3.7   Comparison to Collider Results

The EFT approach theoretically has the potential to allow a comparison between direct detection dark matter experiments and collider searches. Particularly, the relativistic operators relevant for collider searches can be traced back to the set of operators of the non-relativistic effective field theory (a table of this non-relativistic matching can be found in the appendix of [53]).

However, a major assumption made when constructing the non-relativistic effective field theory, is that the mediator is so heavy in comparison to the momentum transfer, that it can be neglected, so that the effective interaction is a four-point interaction. This translation is not straightforward for the relativistic EFT, as momentum transfers are much larger and a four-point interaction is not an accurate description anymore. Instead, the interaction is described in simplified models, where the mediator is exchanged in either the s- or t-channel.
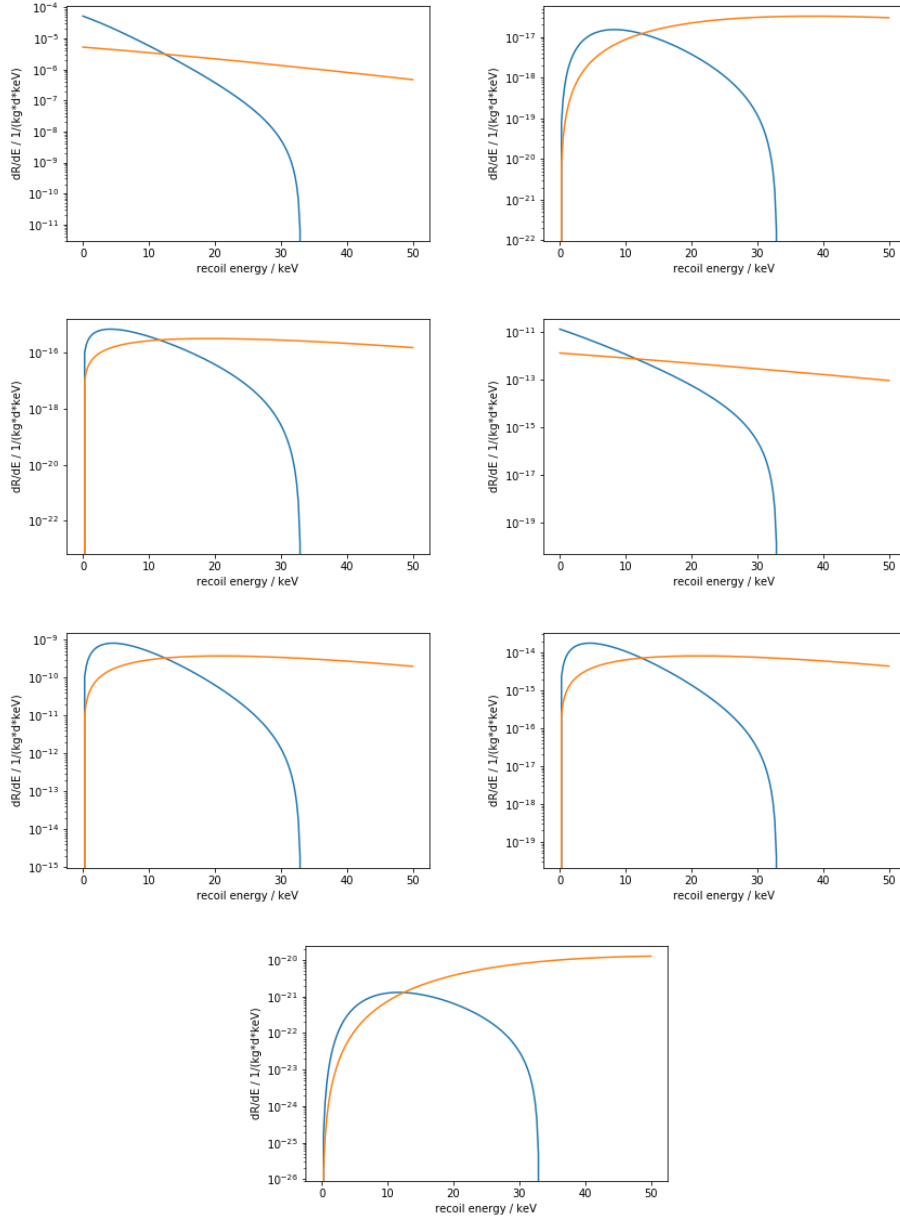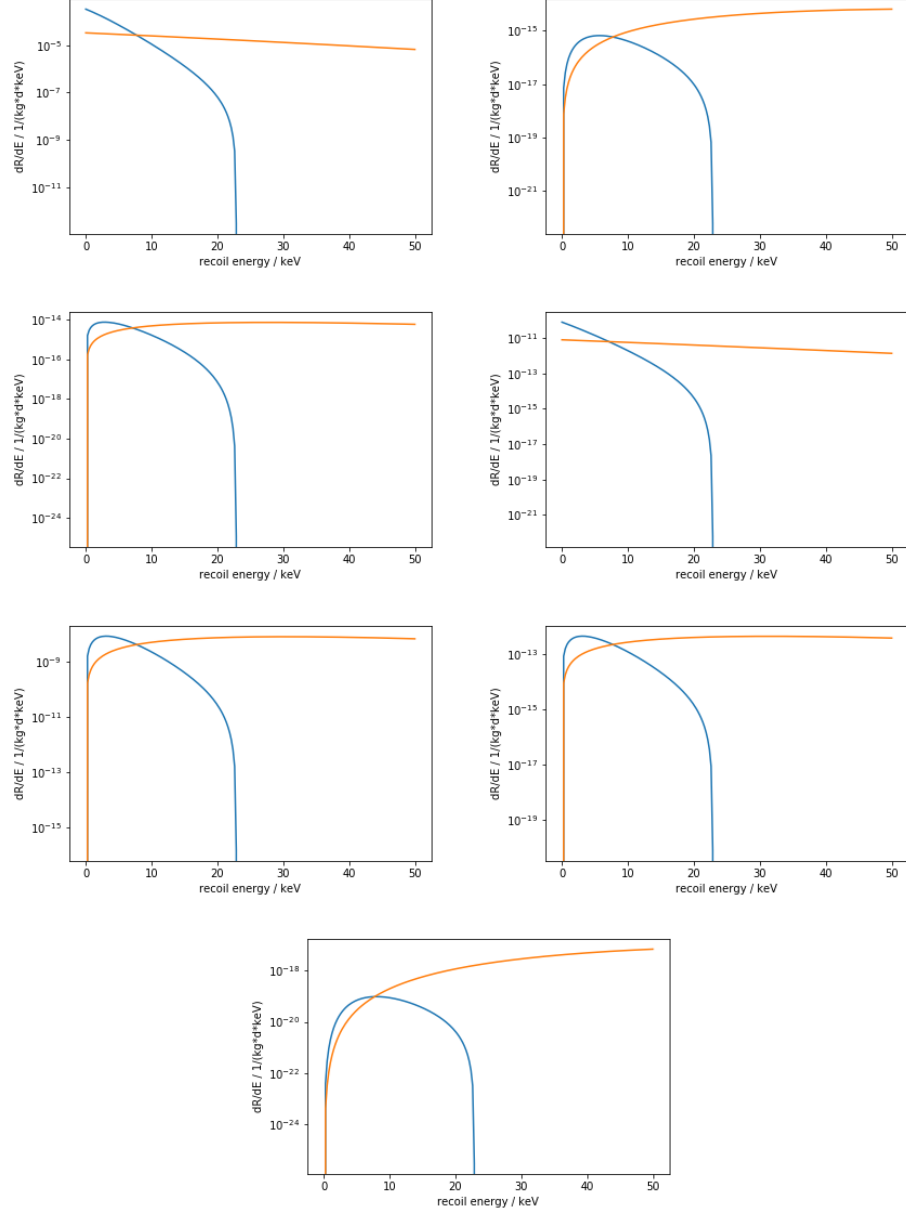
Figure 3.2: Differential spectra for dark matter with a particle mass of $10 \, \text{GeV/c}^2$ (blue) and $100 \, \text{GeV/c}^2$ (orange), scattering off ^{16}O for the EFT operators $\mathcal{O}_1$, $\mathcal{O}_3$, $\mathcal{O}_5$, $\mathcal{O}_8$, $\mathcal{O}_{11}$, $\mathcal{O}_{12}$ and $\mathcal{O}_{15}$.

Figure 3.3: Differential spectra for dark matter with a particle mass of $10\,\mathrm{GeV/c^2}$ (blue) and $100\,\mathrm{GeV/c^2}$ (orange), scattering off $^{40}\mathrm{Ca}$ for the EFT operators $\mathcal{O}_1$, $\mathcal{O}_3$, $\mathcal{O}_5$, $\mathcal{O}_8$, $\mathcal{O}_{11}$, $\mathcal{O}_{12}$ and $\mathcal{O}_{15}$.
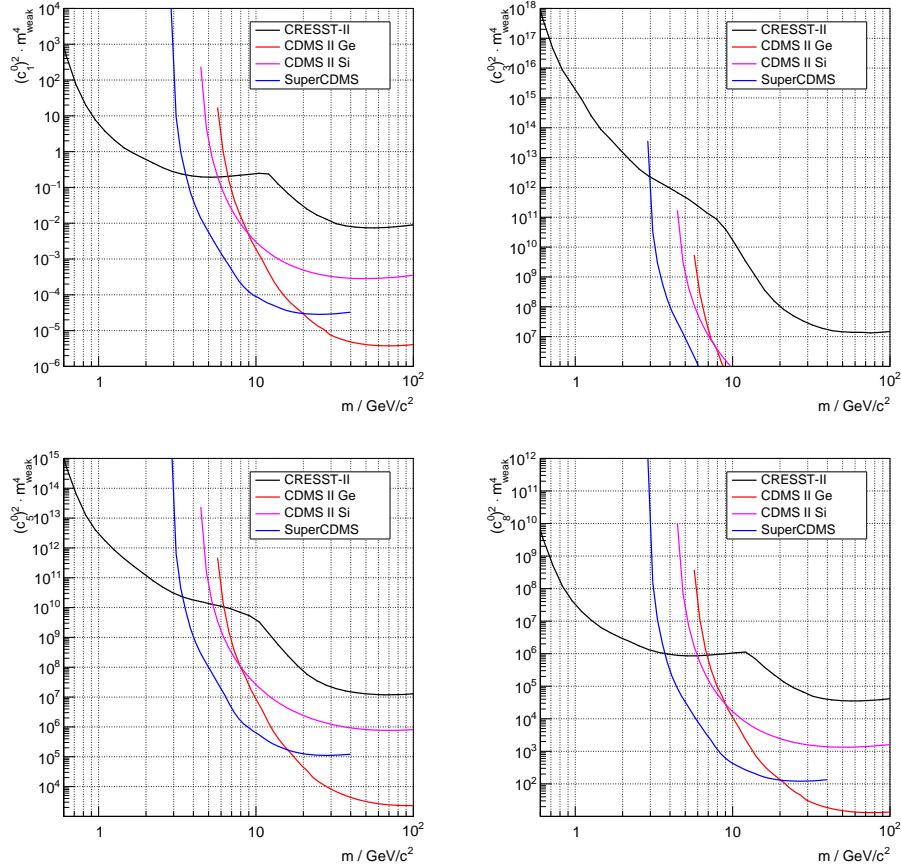
Figure 3.4: Upper 90% limits for the Wilson coefficients c_1^0, c_3^0, c_5^0 and c_8^0 as a function of the dark matter particle mass (black), compared to results from CDMS (CDMS limits from [60]) (other colors). The presented CRESST limits are the result of this work and have been published before in [66]. They are the most sensitive limits for masses below around $3\,\mathrm{GeV/c2}$.
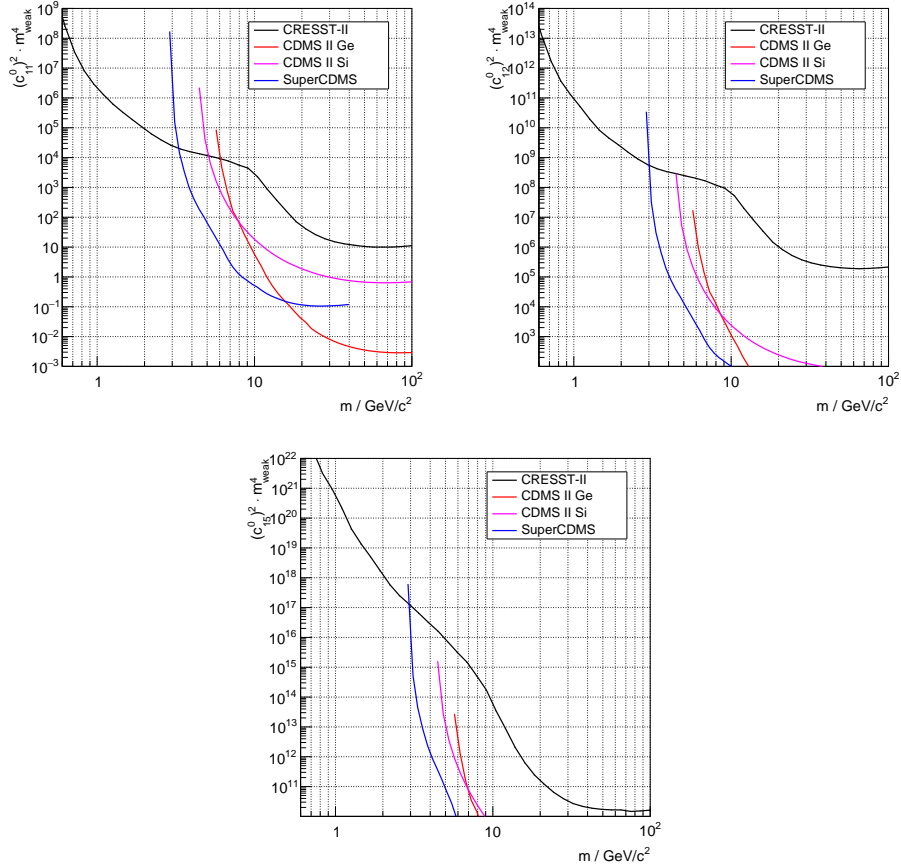
Figure 3.5: Upper 90% limits for the Wilson coefficients c_{11}^0, c_{12}^0 and c_{15}^0 as a function of the dark matter particle mass (black), compared to results from CDMS (CDMS limits from [60]) (other colors). The presented CRESST limits are the result of this work and have been published before in [66]. They are the most sensitive limits for masses below around $3\,\mathrm{GeV/c2}$.

Chapter 4

Conclusions and Outlook

In this work, for the Wilson coefficients c_1^0, c_3^0, c_5^0, c_8^0, c_{11}^0, c_{12}^0 and c_{15}^0 of the effective field theory of dark matter detection, expected recoil spectra specifically for the CRESST-II experiment were calculated and compared to data from the detector *Lise*. All data in the defined region of interested was interpreted to be potentially induced by dark matter and was used to conservatively set limits in the context of the effective theory.

The named coefficients were treated separately, i.e. for each coefficient the spectra were calculated under the assumption that in every case only the corresponding operator contributes to the interaction between the dark matter particle and the nucleon. The CRESST experiment has a low target mass compared to other dark matter experiments, making it less sensitive for more massive particles. However, the experiment also has a very low energy threshold. Consequently, the limits presented in this work are leading for dark matter masses below $3\,\mathrm{GeV/c^2}$, meaning that new parameter space was explored and excluded.

As a next step, the same analysis could be carried out for CRESST-III, which has an even better energy threshold than CRESST-II. Similar to the standard spin-independent results [40], an improvement in the limits especially for very low masses below $1\,\mathrm{GeV/c^2}$ is expected.

The calculation of the spectra is largely based on nuclear considerations and calculations. To further expand the approach presented in this work, a subsequent step could be to include other nuclei in addition to oxygen-16 and calcium-40. For example, the inclusion of oxygen-17, despite of its low natural abundance, would allow to include more EFT operators. In contrast to oxygen-16 and calcium-40, oxygen-17 carries a total nuclear spin, making

it sensitive for operators depending on the nuclear spin, and is additionally sensitive to isovector operators, as it contains a different number of protons and neutrons. Alternatively or complementary, different detector materials could be used. First CRESST results with $LiAlO_2$ crystals [67] showed a high sensitivity to spin-dependent interaction with low-mass dark matter.

Bibliography

[1] J. H. Oort. The force exerted by the stellar system in the direction perpendicular to the galactic plane and some related problems. *Bull.Astron.Inst.Netherlands*, 6:249–287, 1932.

[2] M. Crézé et al. The distribution of nearby stars in phase space mapped by Hipparcos: I. The potential well and local dynamical mass. *Astron.Astrophys.*, 329:920, 1998.

[3] F. Zwicky. Die Rotverschiebung von extragalaktischen Nebeln. *Helvetica Physica Acta*, 6:110–127, 1933.

[4] A. Bosma. 21-cm line studies of spiral galaxies. I - Observations of the galaxies NGC 5033, 3198, 5055, 2841, and 7331. *Astronomical Journal*, 86:1791–1824, 1981.

[5] V. Rubin et al. Rotation Velocities of 16 SA Galaxies and a Comparison of Sa, Sb, and SC Rotation Properties. *The Astrophysical Journal*, 289:81–104, 1985.

[6] P. Salucci. The mass distribution in Spiral galaxies. *IAU Symp.*, 244:53–62, 2008.

[7] J. A. Tyson et al. Detailed mass map of CL0024+1654 from strong lensing. *Astrophys.J.Lett.*, 498:L107, 1998.

[8] M. Milgrom. A modification of the Newtonian dynamics as a possible alternative to the hidden mass hypothesis. *Astrophysical Journal*, 270:365–370, 1983.

[9] D. Clowe et al. A direct empirical proof of the existence of dark matter. *Astrophys.J.Lett.*, 648:L109–L113, 2006.

[10] B. Carr et al. Primordial Black Holes as Dark Matter. *Phys.Rev.D*, 94:083504, 2016.

[11] C. L. Bennett et al. Nine-Year Wilkinson Microwave Anisotropy Probe (WMAP) Observations: Final Maps and Results. *Eur. Phys. J. C*, 79:43, 2019.

[12] V. Springel et al. Simulations of the formation, evolution and clustering of galaxies and quasars. *Nature*, 435:629–636, 2005.

[13] K. Freese. Status of Dark Matter in the Universe. *Int.J.Mod.Phys.*, 1(06):325–355, 2017.

[14] M. S. Roberts and R. N. Wihitehurst. The rotation curve and geometry of M31 at large galactocentric distances. *Astrophysical Journal*, 201:327–346, 1975.

[15] M. Aker et al. An improved upper limit on the neutrino mass from a direct kinematic method by KATRIN. *Phys.Rev.Lett.*, 123(22):221802, 2019.

[16] L. Roszkowski et al. WIMP dark matter candidates and searches – current status and future prospects. *Rept.Prog.Phys.*, 81(6):066201, 2018.

[17] J. L. Feng. Dark Matter Candidates from Particle Physics and Methods of Detection. *Ann.Rev.Astron.Astrophys.*, 48:495–545, 2010.

[18] T. Flacke et al. Electroweak Kaluza-Klein Dark Matter. *JHEP*, 04:041, 2017.

[19] J. A. R. Cembranos et al. Cosmological and astrophysical limits on brane fluctuations. *Phys.Rev.D*, 68:103505, 2003.

[20] K. Agashe and G. Servant. Warped unification, proton stability and dark matter. *Phys.Rev.Lett.*, 93:231805, 2004.

[21] A. Birkedal et al. Little Higgs dark matter. *Phys.Rev.D*, 74:0235002, 2006.

[22] M. Garny and J. Heisig. Interplay of super-WIMP and freeze-in production of dark matter. *Phys.Rev.D*, 98(9):095031, 2018.

[23] J. A. R. Cembranos et al. Brane world dark matter. *Phys.Rev.Lett.*, 90:241301, 2003.

[24] R. D. Peccei and H. R. Quinn. CP Conservation in the Presence of Pseudoparticles. *Phys.Rev.Lett.*, 38:1440–1443, 1977.

[25] L. Bergstrom. Dark Matter Candidates. *New J.Phys.*, 11:105006, 2009.

[26] A. Boyarsky et al. Sterile neutrino Dark Matter. *Prog.Part.Nucl.Phys.*, 104:1–45, 2019.

[27] M. Tanabashi and others (Particle Data Group). Sterile neutrino Dark Matter. *Prog.Part.Nucl.Phys.*, 104:1–45, 2019.

[28] R. H. Helm. Inelastic and Elastic Scattering of 187-Mev Electrons from Selected Even-Even Nuclei. *Phys.Rev.*, 104:1466–1475, 1956.

[29] J. D. Lewin and P. F. Smith. Review of mathematics, numerical factors, and corrections for dark matter experiments based on elastic nuclear recoil. *Astropart.Phys.*, 6:87–112, 1996.

[30] T. M. Undagoitia and L. Rauch. Dark matter direct-detection experiments. *J.Phys.G*, 43(1):013001, 2016.

[31] M. C. Smith et al. The RAVE Survey: Constraining the Local Galactic Escape Speed. *Mon.Not.Roy.Astron.Soc.*, 379:755–772, 2007.

[32] T. Piffl et al. The RAVE survey: the Galactic escape speed and the mass of the Milky Way. *Astron. Astrophys.*, 562:A91, 2014.

[33] N. W. Evans and J. H. An. Distribution function of the dark matter. *Phys.Rev.D*, 73:023524, 2006.

[34] C. Kelso. The impact of baryons on the direct detection of dark matter. *JCAP*, 08:071, 2016.

[35] XENON Collaboration: E. Aprile et al. Dark Matter Search Results from a One Ton-Year Exposure of XENON1T. *Phys.Rev.Lett.*, 121(11):111302, 2018.

[36] LUX Collaboration: D. S. Akerib et al. Improved Limits on Scattering of Weakly Interacting Massive Particles from Reanalysis of 2013 LUX data. *Phys.Rev.Lett.*, 116(16):161301, 2016.

[37] PandaX-II Collaboration: X. Cui et al. Dark Matter Results From 54-Ton-Day Exposure of PandaX-II Experiment. *Phys.Rev.Lett.*, 119(18):181302, 2017.

[38] Official image of the CRESST Collaboration.

[39] CRESST Collaboration: A. H. Abdelhameed et al. Description of CRESST-III Data. *arXiv:1905.07335*, 2019.

[40] CRESST Collaboration: A. H. Abdelhameed et al. First results from the CRESST-III low-mass dark matter program. *Phys.Rev.D*, 100(10):102002, 2019.

[41] R. Strauss et al. Energy-dependent light quenching in $CaWO_4$ crystals at mK temperatures. *Eur.Phys.J.C*, 74(7):2957, 2014.

[42] S. P. Ahlen et al. Limits on Cold Dark Matter Candidates from an Ultralow Background Germanium Spectrometer. *Physics Letters B*, 195(4):603–608, 1987.

[43] DAMA Collaboration: R. Bernabei et al. First results from DAMA/LIBRA and the combined results with DAMA/NaI. *Eur.Phys.J.C*, 56:333–355, 2008.

[44] CoGeNT Collaboration: C. E. Aalseth et al. CoGeNT: A Search for Low-Mass Dark Matter using p-type Point Contact Germanium Detectors. *Phys.Rev.D*, 88:012002, 2013.

[45] H. Abdalla et al. Searches for gamma-ray lines and pure WIMP spectra from Dark Matter annihilations in dwarf galaxies with H.E.S.S. *JCAP*, 11:037, 2018.

[46] ATLAS Collaboration: M. Aaboud et al. Constraints on mediator-based dark matter and scalar dark energy models using $\sqrt{s} = 13$ TeV pp collision data collected by the ATLAS detector. *JHEP*, 05:142, 2019.

[47] A. Zhitnitsky. DAMA/LIBRA annual modulation and Axion Quark Nugget Dark Matter Model. *Phys.Rev.D*, 101(8):083020, 2019.

[48] S. Kang et al. Anapole Dark Matter after DAMA/LIBRA-phase2. *JCAP*, 11:040, 2018.

[49] D. Tucker-Smith and N. Weiner. Inelastic dark matter. *Phys.Rev.D*, 64:043502, 2001.

[50] S. Chang et al. Inelastic Dark Matter in Light of DAMA/LIBRA. *Phys.Rev.D*, 79:043513, 2009.

[51] S. Chang et al. Momentum Dependent Dark Matter Scattering. *JCAP*, 01:006, 2010.

[52] J. Fan et al. Non-relativistic effective theory of dark matter direct detection. *JCAP*, 11:042, 2010.

[53] A. L. Fitzpatrick et al. The Effective Field Theory of Dark Matter Direct Detection. *JCAP*, 02:004, 2013.

[54] A. L. Fitzpatrick et al. Model Independent Direct Detection Analyses. *arXiv:1211.2818*, 2012.

[55] N. Anand et al. Weakly interacting massive particle-nucleus elastic scattering response. *Phys.Rev.C*, 89(6):065501, 2014.

[56] R. Catena and B. Schwabe. Form factors for dark matter capture by the Sun in effective theories. *JCAP*, 04:042, 2015.

[57] M. Weber and W. de Boer. Determination of the Local Dark Matter Density in our Galaxy. *Astron. Astrophys.*, 509:A25, 2010.

[58] J. Meija et al. Isotopic compositions of the elements (IUPAC Technical Report). *Pure and Applied Chemistry*, 88(3), 2013.

[59] IUPAC Periodic Table of the Elements.

[60] SuperCDMS Collaboration: K. Schneck et al. Dark matter effective field theory scattering in direct detection experiments. *Phys.Rev.D*, 91(9):092004, 2015.

[61] CRESST Collaboration: G. Angloher et al. Description of CRESST-II data. *arXiv:1701.08157*, 2017.

[62] CRESST Collaboration: G. Angloher et al. Results on light dark matter particles with a low-threshold CRESST-II detector. *Eur.Phys.J.C*, 76(1):25, 2016.

[63] S. Yellin. Finding an upper limit in the presence of unknown background. *Phys.Rev.D*, 66:032005, 2002.

[64] S. Yellin. Extending the optimum interval method. *arXiv:0709.2701*, 2008.

[65] XENON Collaboration: E. Aprile et al. Effective field theory search for high-energy nuclear recoils using the XENON100 dark matter detector. *Phys.Rev.D*, 96(4):042004, 2017.

[66] G. Angloher et al. Limits on dark matter effective field theory parameters with CRESST-II. *Eur. Phys. J. C*, 79:43, 2019.

[67] CRESST Collaboration: A. H. Abdelhameed et al. Cryogenic characterization of a $LiAlO_2$ crystal and new results on spin-dependent dark matter interactions with ordinary matter. *arXiv:2005.02692*, 2020.

Danksagung

Ich möchte mich herzlich bei Prof. Josef Jochum bedanken, dass er mir die Möglichkeit gegeben hat diese Arbeit unter seiner Aufsicht durchzuführen, sowie für die Betreuung in diesen Jahren. Ebenso bedanke ich mich bei Prof. Tobias Lachenmaier als Zweitgutachter und Zweitbetreuer. Bei beiden und ihren gesamten Arbeitsgruppen möchte ich mich auch insbesondere für die angenehme Arbeitsatmosphäre bedanken, sodass die Zeit am Institut auch viel Spaß gemacht hat.

Hervorzuheben aus der Arbeitsgruppe sind besonders Christian, der in der Regel mein erster Ansprechpartner in Bezug auf das CRESST-Experiment und die Datenanalyse war, außerdem Gaby für alle organisatorischen Dinge, sowie meine dauerhafte Schreibtischnachbarin Büsra.

Außerhalb Tübingens bedanke ich mich auch bei der restlichen CRESST-Kollaboration, sowie bei Prof. Riccardo Catena für die Zusammenarbeit.

Aus dem privaten Bereich haben mich meine Eltern und meine Geschwister in jeglicher Hinsicht immer unterstützt und somit auch zu dieser Arbeit beigetragen. Während der Tübinger Zeit kamen außerdem Eva und auch ihre Familie dazu, vielen Dank dafür!